

A First-Principles Study of the Electronic Reconstructions of LaAlO₃/SrTiO₃ Heterointerfaces and Their Variants

Hanghui Chen^{1,3} Alexie Kolpak^{2,3} and Sohrab Ismail-Beigi^{1,2,3}

¹*Department of Physics, Yale University,
New Haven, Connecticut, 06511, USA*

²*Department of Applied Physics, Yale University,
New Haven, Connecticut, 06511, USA*

³*Center for Research on Interface Structures and Phenomena (CRISP),
Yale University, New Haven, CT 06511, USA*

(Dated: October 29, 2018)

Abstract

We present a first-principles study of the electronic structures and properties of ideal (atomically sharp) LaAlO₃/SrTiO₃ (001) heterointerfaces and their variants such as a new class of quantum well systems. We demonstrate the insulating-to-metallic transition as a function of the LaAlO₃ film thickness in these systems. After the phase transition, we find that conduction electrons are bound to the *n*-type interface while holes diffuse away from the *p*-type interface, and we explain this asymmetry in terms of a large hopping matrix element that is unique to the *n*-type interface. We build a tight-binding model based on these hopping matrix elements to illustrate how the conduction electron gas is bound to the *n*-type interface. Based on the ‘polar catastrophe’ mechanism, we propose a new class of quantum wells at which we can manually control the spatial extent of the conduction electron gas. In addition, we develop a continuous model to unify the LaAlO₃/SrTiO₃ interfaces and quantum wells and predict the thickness dependence of sheet carrier densities of these systems. Finally, we study the external field effect on both LaAlO₃/SrTiO₃ interfaces and quantum well systems. Our systematic study of the electronic reconstruction of LaAlO₃/SrTiO₃ interfaces may serve as a guide to engineering transition metal oxide heterointerfaces.

I. INTRODUCTION

With the advance of techniques to control thin film growth on the atomic scale, the study of epitaxial oxide heterostructures is a rapidly developing area of materials science [1]. Due to the ability to produce a well-defined single terminated substrate surface [2], interfaces that are nearly atomically sharp can be formed. In many cases, the properties of these interfaces turn out to be much richer than those of the bulk constituents. One of the most interesting examples is the (001) interface between LaAlO_3 (LAO) and SrTiO_3 (STO), both constituents of which are conventional band insulators in the bulk. Among the intriguing phenomena observed at this interface is the presence of a high-mobility quasi two-dimensional electron gas [3], which is sensitive to the LaAlO_3 film thickness on the nanoscale [4-6], and can be tuned via an external field [4, 7]. In addition, both magnetism [8] and superconductivity [9] have been observed at $\text{LaAlO}_3/\text{SrTiO}_3$ interfaces.

Due to these interface properties, the $\text{LaAlO}_3/\text{SrTiO}_3$ system shows great promise for the development of novel applications in nano-scale oxide electronics [10, 11]. However, though significant efforts have been made in both theory [12-18] and experiment [19-25], the origin of the new phases emerging at the $\text{LaAlO}_3/\text{SrTiO}_3$ interface has not been completely resolved yet. In part, this is due to the fact that more than one mechanism may play a role in determining the behavior, and furthermore, the dominant mechanism can depend on external conditions [26].

One mechanism that is generally believed to play a role in the formation of the two-dimensional electron gas is known as the polar catastrophe. This mechanism is a direct result of the charge discontinuity that occurs at an abrupt interface between a nonpolar (SrTiO_3) and a polar (LaAlO_3) material. Both materials are perovskite oxides with an ABO_3 structure that forms alternating planes of AO and BO_2 stacked along the (001) direction. Consequently, there are two types of $\text{LaAlO}_3/\text{SrTiO}_3$ interfaces along this direction: TiO_2/LaO (known as the n -type interface) and SrO/AlO_2 (the p -type interface) [3, 27]. In the ionic limit, SrTiO_3 is composed of charge neutral atomic layers $(\text{SrO})^0$ and $(\text{TiO}_2)^0$, while LaAlO_3 consists of positively charged $(\text{LaO})^+$ and negatively charged $(\text{AlO})^-$ atomic layers. When LaAlO_3 is grown epitaxially on the SrTiO_3 substrate along the (001) direction, an internal electric field directed from $(\text{LaO})^+$ to $(\text{AlO}_2)^-$ is formed through LaAlO_3 , resulting in a potential difference that, mathematically, diverges with increasing LaAlO_3

thickness. In reality, to offset the diverging potential, an electronic reconstruction is expected to occur, with electrons transferring from the film surface (or a p -type interface) to the n -type interface. The polar catastrophe mechanism [3, 27] has been confirmed in density functional theory (DFT) calculations [18, 28–30], and could be responsible for the presence of the two-dimensional electron gas at the atomically sharp n -type interface (i.e., with no defects).

However, the polar catastrophe mechanism alone can not explain all of the electronic properties of the $\text{LaAlO}_3/\text{SrTiO}_3$ interface, such as the observed confinement of the transferred electrons within several nanometers of the n -type interface [31]. In previous work [28], we have shown that the electrons are bound to the n -type interface as a result of the chemical environment of the interface, which produces a large hopping matrix element between La and Ti.

In this paper, we use both DFT and phenomenological modeling to provide a more detailed and complete picture of the electronic reconstruction at ideal $\text{LaAlO}_3/\text{SrTiO}_3$ interfaces. We predict the behavior of the sheet carrier density as a function of the LaAlO_3 thickness by constructing a continuous model which approximates the LaAlO_3 as a homogeneous media. We also use both DFT calculations and model calculations to give a simple yet quantitative picture of the external field effect that has been experimentally realized at the n -type interface [4, 7]. In addition, we propose a new class of quantum well systems, based on the polar catastrophe mechanism, at which the spatial extent of the two-dimensional electron gas can be manually controlled.

The remainder of the paper is organized as follows. In Section II, we discuss the technical details of our DFT calculations. We present our first-principles results in Section III. Section III A gives a brief discussion on the symmetric superlattices. In III B, we briefly describe the polar catastrophe at various types of interfaces, and we introduce the new quantum well systems. Section III C discusses the computation of the on-site and hopping matrix elements and a tight-binding model. An exceptionally large Ti-La hopping is found at the n -type interface and its origin is explained. Section III D studies the behavior of oxygen vacancies at the interfaces. Section III E examines the thickness dependence of the sheet carrier density. Simulations of the external field effect are presented in III F. In Section IV, we present a continuous model which gives a simple yet quantitative description of both the sheet carrier density and the external field effect. We conclude in Section V.

II. METHOD DETAILS

Our calculations are performed using density functional theory within the *ab initio* supercell plane-wave approach [32], with the code PWscf in the Quantum-ESPRESSO package [52]. We employ the local density approximation (LDA) [33] and ultrasoft pseudopotentials [34], which include semi-core states in Sr, Ti and La. The reference configurations of the pseudopotentials are: Sr $4s^2 4p^6 5s^2$ ($r_c^s = 2.0a_0, r_c^p = 1.8a_0$), Ti $3s^2 3p^6 3d^1 4s^2$ ($r_c^s = r_c^p = r_c^d = 1.8a_0$), La $5s^2 5p^6 5d^1 6s^{1.5} 6p^{0.5}$ ($r_c^s = r_c^d = 2.2a_0, r_c^p = 2.0a_0$), Al $3s^2 3p^1$ ($r_c^s = 1.8a_0, r_c^p = 1.82a_0$) and O $2s^2 2p^4$ ($r_c^s = r_c^p = 1.3a_0$), where a_0 is the Bohr radius. The plane wave basis energy cutoff and charge cutoff are 30 Ry and 180 Ry, respectively. We use a Gaussian smearing width of 5 mRy when sampling the Brillouin zone. The k -grid sampling of the Brillouin zone is $10 \times 10 \times 1$ where the z -axis is orthogonal to the interface. The convergence of the total energy and total charge density has been checked with k -grids of up to $20 \times 20 \times 1$. Periodic copies are separated by $\sim 15 \text{ \AA}$ of vacuum. We also extend the vacuum to 30 \AA to check the convergence. The effect of the artificial electric fields in the vacuum due to the periodic boundary condition, which turns out to be quite small, is discussed in Appendix B 1. The force convergence threshold is 26 meV/\AA . In some key results we reduce the threshold to 13 meV/\AA to check the convergence.

In all our calculations, the interfaces are along the (001) direction so that the z axis is perpendicular to the interface. The x and y directions of the simulation cell are subject to periodic boundary conditions and their lengths are fixed to the theoretical lattice constant of SrTiO₃ $a = 3.85 \text{ \AA}$ (1.5% smaller than the experimental value). The atomic coordinates are relaxed [53] until every force component is smaller than the convergence threshold. The detailed configurations for different calculations are specified in each section below.

III. DFT RESULTS

A. Symmetric double n -type and p -type superlattices

The simplest approach to studying the n -type or p -type SrTiO₃/LaAlO₃ interface is to use a symmetric superlattice approach [12–17, 35–37], as exemplified by Fig. 1, which shows a simulation cell without vacuum in which a number of SrTiO₃ unit cells are adjacent to a number of LaAlO₃ unit cells and periodic boundary conditions are imposed. Therefore,

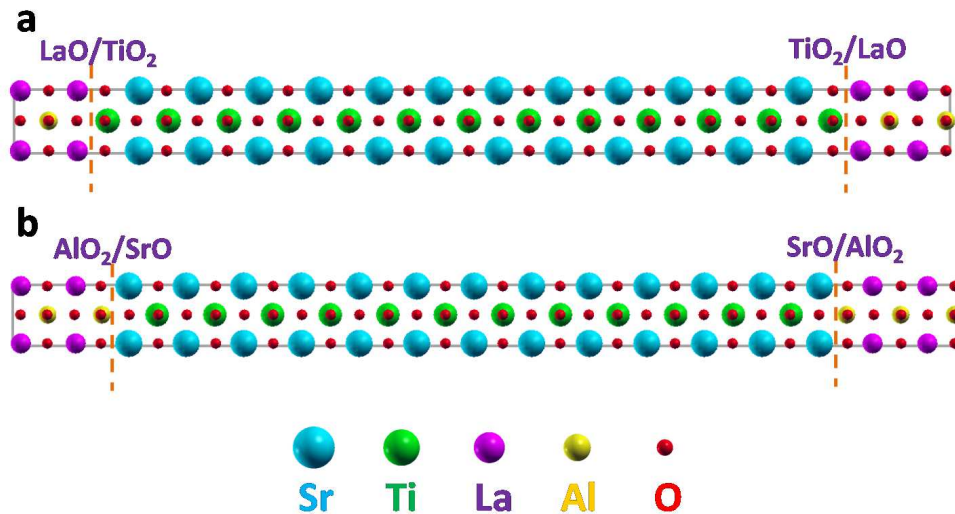


FIG. 1: Schematics of symmetric superlattices. **a)** The double n -type superlattice. **b)** The double p -type superlattice. The interface is highlighted by the dashed line.

a non-stoichiometric supercell contains two identical SrTiO₃/LaAlO₃ interfaces: *e.g.* in Fig. 1a, we have an additional TiO₂ layer in SrTiO₃ and an additional LaO layer in LaAlO₃, and in Fig. 1b, there is an additional SrO layer in SrTiO₃ and an additional AlO₂ in LaAlO₃. In this way, the superlattice contains two n -type interfaces (TiO₂/LaO) or two p -type interfaces (SrO/AlO₂).

The advantage of the superlattice approach is that no vacuum is needed in the simulation cell, making computation easier. However, due to the imposed symmetry and non-stoichiometry of the LaAlO₃ film, this geometry does not result in a polar field, so the evolution of the polar catastrophe can not be modeled. In addition, the non-stoichiometry of the LaAlO₃ also imposes a fixed carrier doping: in the ionic limit, an LaO (AlO₂) layer has a charge of +1 (-1), and there is one extra electron (hole) present in the conduction (valence) band of LaAlO₃, which is shared evenly by the two interfaces. Therefore each interface is doped by 0.5 electrons (n -type) or 0.5 holes (p -type) per two-dimensional unit cell. These values are precisely those needed to fully compensate the polar field of LaAlO₃ [27], so the symmetric supercell approach is equivalent to studying the properties of the interfaces when the LaAlO₃ film is very thick (infinite thickness limit).

We briefly present results on the symmetric interfaces and highlight some key observations and questions that we will answer in later sections. We show in Fig. 2a the xy -plane integrated *conduction* electron density for the double n -type superlattice, and in Fig 2b

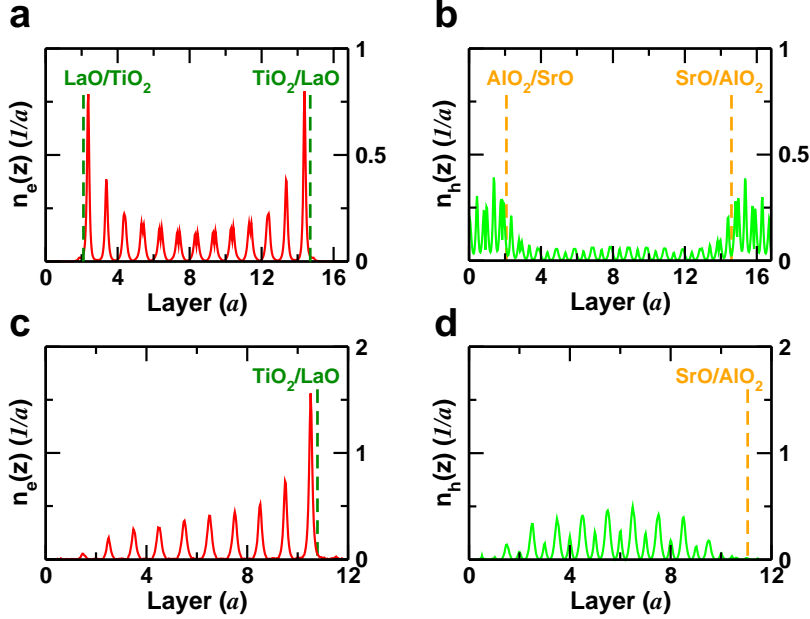


FIG. 2: Transferred electron and hole densities integrated over the xy plane. In each panel, the integral of the conduction electron/hole density is normalized to unity. The layers are measured in units of the SrTiO_3 lattice constant a . **a)** The symmetric n -type superlattice. The electrons are bound to the n -type interface. **b)** The symmetric p -type superlattice. The holes reside in both the SrTiO_3 and LaAlO_3 layers. **c)** The n -type interface with 4 u.c. of LaAlO_3 . The electrons decay away from the n -type interface. **d)** The p -type interface with 5 u.c. of LaAlO_3 . The holes, driven by the polar field through LaAlO_3 , diffuse into the SrTiO_3 substrate. Appendix A explains in detail how to calculate these transferred charge densities.

the hole density for the double p -type superlattice. The method of how to calculate the transferred charge density is detailed in Appendix A. The integrated densities are 0.49 electrons per n -type interface and 0.49 holes per p -type interface, showing that the ionic picture for LaAlO_3 is highly accurate, and that one should expect 0.5 electrons (holes) at the fully compensated n -type (p -type) interface for very thick LaAlO_3 films.

The density profiles in Fig. 2 display an interesting asymmetry. One can characterize the electrons in the double n -type system as being bound to the interface. As the figure shows, they are confined in the SrTiO_3 , with the density decreasing away from the interface. On the other hand, in the double p -type system, the holes reside in both the LaAlO_3 and

SrTiO₃, do not show a strong preference for the interface itself, and have a slightly higher amplitude in the LaAlO₃.

Our calculated band offsets place the LaAlO₃ valence band maximum $\simeq 0.1$ eV above the SrTiO₃ valence band maximum (*p*-type) and the LaAlO₃ conduction band minimum ~ 2 eV above the SrTiO₃ conduction band minimum (*n*-type) [13, 15]. *A priori*, one would expect that any introduced carriers would occupy the most energetically favorable band edge available, *i.e.* holes would migrate to the LaAlO₃ valence band edge and electrons to the SrTiO₃ conduction band edge. Furthermore, the minimization of kinetic energy would lead to a relatively uniform distribution of carriers. In Fig. 2, we see that, overall, the holes prefer to be in the LaAlO₃ at the *p*-type interface, while the electrons reside in SrTiO₃ at the *n*-type interface. For the *p*-type interface, the small value of the band offset and the large hole density result in some “leakage” into the SrTiO₃ valence band states.

However, the binding of the electrons at the *n*-type interface cannot be explained by the above arguments. As no polar fields are present in this system to create a potential that will bind the electrons, what mechanism overcomes the kinetic cost inherent in localizing them to the interface? Whatever mechanism is present is absent for the holes, whose spatial profile is relatively uniform in both materials. We provide the answer to this fundamental question in Section III C, when we discuss the tight-binding hopping matrix elements across both interfaces.

Before we move onto the next section, we would like to give a short discussion on the valence band offset (VBO) of LaAlO₃/SrTiO₃ interfaces. The VBO of the *n*-type interface has been calculated by several groups [10, 13, 15, 37, 38]. Although all of the computed values place the conduction band edge of LaAlO₃ significantly higher than that of SrTiO₃ at the *n*-type interface, the large range of computed VBO values (shown in Table I), is puzzling. To investigate this issue, we use two different approaches to calculate the VBO of the *n*-type interface and the *p*-type interface. The valence band offset is defined by:

$$E_{\text{VBO}} = E_{\text{V}}^{\text{LAO}} - E_{\text{V}}^{\text{STO}} \quad (1)$$

where $E_{\text{V}}^{\text{LAO}}$ and $E_{\text{V}}^{\text{STO}}$ are the valence band edges of LaAlO₃ and SrTiO₃, respectively. The simulation cell is a symmetric nonstoichiometric superlattice with 12.5 layers of SrTiO₃ and 4.5 layers of LaAlO₃. The first method to determine the VBO is to analyze the local density of states, referred to as the LDOS approach [15, 39]. The other method is to use

the macroscopic average potential, denoted further as the MA approach [15, 40, 41]. We compare our results with other theoretical calculations and the recent experiment in Table I.

TABLE I: The valence band offset (VBO) of $\text{LaAlO}_3/\text{SrTiO}_3$ n -type and p -type interfaces in eV. Each value is followed by the method used to determine it in parentheses.

	n -type (TiO_2/LaO)	p -type (SrO/AlO_2)
present study	-0.47 (MA) -0.39 (LDOS)	-0.02 (MA) 0.11 (LDOS)
Ref. [15]	0.51 (MA) 0.39 (LDOS)	0.19 (MA) 0.10 (LDOS)
Ref. [10]	1.1	NA
Ref. [13]	-0.15 (LDOS)	NA
Ref. [37]	-0.9 (LDOS)	NA
Ref. [38]	-0.1 (MA)	NA
Expt. [42]	-0.35 ± 0.18	NA

We can see from Table I that for the n -type interface not only the magnitude of VBO differs, but the sign is not unanimous. One possible origin for the range of theoretical values is likely that the lattice constants have minute differences (due to different pseudopotentials), which causes a variation in strain and probably affects the alignment of valence band edges. Another possibility is that we, as well as a few other groups [13, 15, 37, 38], use symmetric nonstoichiometric superlattices, in which the macroscopic average potentials are flat in both LaAlO_3 and SrTiO_3 , to perform the calculations. However, if a stoichiometric LaAlO_3 slab is employed [10] so that a net internal electric field results, the determined VBO will likely be different from the symmetric nonstoichiometric case. Although our results for the n -type interface agree well with the available experiments, the value as well as variations of the VBO for the n -type interface is not a closed subject and needs further work. In contrast, the computed values of the VBO for the p -type interface are in general agreement and $\simeq 0.1$ eV.

B. The polar catastrophe

1. *n*-type, *p*-type and *np*-type interfaces

As discussed in the Introduction, there are two types of $\text{LaAlO}_3/\text{SrTiO}_3$ interfaces: the *n*-type (TiO_2/LaO) interface and the *p*-type (SrO/AlO_2) interface. If a stoichiometric LaAlO_3 layer on an SrTiO_3 substrate also has a SrTiO_3 capping layer, then we have both *n*-type and *p*-type interfaces in the same system. Below, we refer to this type of geometry as the *np*-type interface. Experimentally, the *n*-type, *p*-type and *np*-type interfaces have all been fabricated. In this study, we simulate all three types of interfaces, the configurations of which are illustrated in Fig. 3. For the *np*-type interface, we use 5 unit cells of SrTiO_3 to simulate the substrate and another 5 unit cells of SrTiO_3 as a capping layer. For both the *n*-type and *p*-type interfaces, we use 11 unit cells of SrTiO_3 to simulate the substrate. In all cases, the thickness of LaAlO_3 is varied from 1 to 7 unit cells. In addition, the first two SrTiO_3 unit cells in the substrate are fixed at the ideal perovskite positions to simulate the bulk-like interior of the substrate [28]. The termination of the SrTiO_3 substrate and capping layers is always SrO. As illustrated in our previous work [54], the TiO_2 termination has a surface O-*p* state which is $\simeq 0.5$ eV higher than the valence band edge of bulk SrTiO_3 , while the SrO termination does not have this surface state. Since we are interested in the evolution of polar fields of LaAlO_3 on very thick SrTiO_3 substrates, this pure surface state should be avoided when simulating the SrTiO_3 substrate and thick SrTiO_3 capping layers. However, for thin SrTiO_3 capping layers, the presence of this O-*p* state on the TiO_2 -terminated surface will lower the critical separation, which has recently been discussed [43].

We observe that an insulating-to-metallic transition occurs in our simulations when the LaAlO_3 film reaches a critical thickness, the value of which depends on the system geometry. The phase transition can be explained in terms of an energy diagram shown in Fig. 3. For the *np*-type and *n*-type interfaces, due to the polar structure of LaAlO_3 , the electric field through the LaAlO_3 film lifts up the valence band edge of the LaAlO_3 and reduces the energy gap. The energy gap of the *np*-type interface is the energy difference between the Ti-*d* states of the SrTiO_3 substrate and the O-*p* states of the SrTiO_3 capping layer, while the energy gap of the *n*-type interface is given by the energy difference between the Ti-*d* states of the SrTiO_3 substrate and the O-*p* states on the surface. For the *p*-type interface,

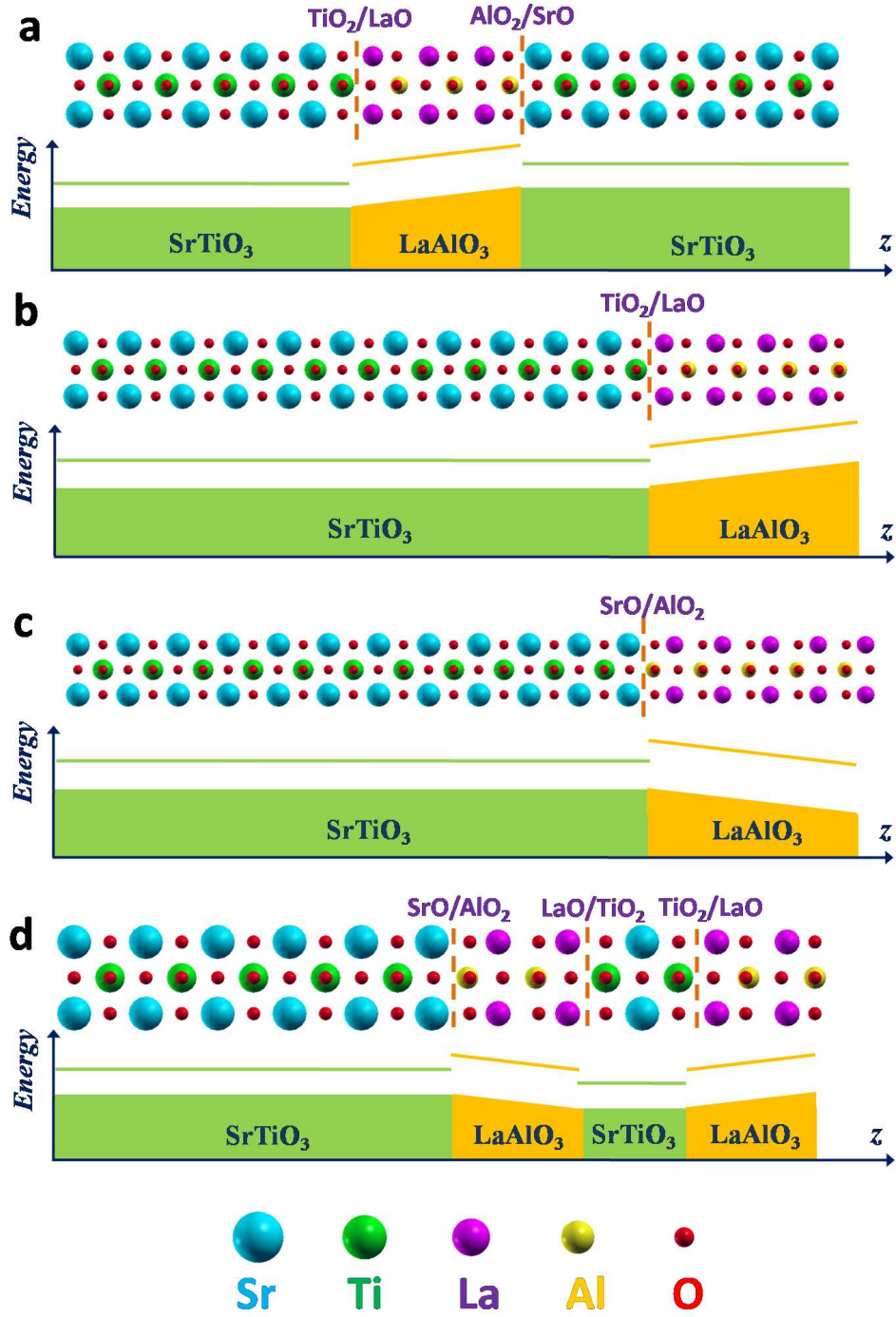


FIG. 3: Schematics of the supercells and energy diagrams for different types of interfaces. **a)** The *np*-type interface. **b)** The *n*-type interface. **c)** The *p*-type interface. **d)** The new quantum well systems.

since the polarity of LaAlO_3 is reversed, the electric field through the LaAlO_3 film decreases the valence band edge of the LaAlO_3 . However, the energy gap of the p -type interface is not the most relevant quantity to monitor for the insulating-to-metallic transition. Rather, the LaAlO_3 film reduces the energy difference between the La states on the surface [55] and the O p -states of the SrTiO_3 substrate, which from now on we call the ‘La-O energy difference’. In all three cases, the energy gap (np -type and n -type) or La-O energy difference (p -type) diminishes with the LaAlO_3 film thickness, finally disappearing when the insulating-to-metallic transition occurs. The minimum number of LaAlO_3 unit cells necessary to induce this phase transition is referred to as the ‘critical separation’.

Our DFT calculations, as well as previous studies [18, 28–30], support the above schematics. The values of the calculated energy gap versus the LaAlO_3 thickness are listed in Table II for the np -type, n -type and p -type interfaces. The corresponding ‘critical separation’ is the smallest thickness of LaAlO_3 that makes the interface conducting. The increasing thickness of the LaAlO_3 film reduces the energy gap until it disappears and the interface becomes metallic. However, the critical separation depends on the band gap of SrTiO_3 , which is underestimated in DFT calculations (the calculated band gap is 1.85 eV and the experimental band gap is 3.2 eV). Taking into account the difference between the calculated and experimental band gaps, the realistic critical separation is two more unit cells of LaAlO_3 in addition to the calculated one, resulting in 5, 6 and 8 u.c. for the np -type, n -type and p -type interfaces, respectively.

In order to give a clearer illustration of how the polar field reduces the energy gap, we show in the left column of Fig. 4, the xy planar average electrostatic potential [40] and the associated macro-averaged smoothed potential along the direction perpendicular to the interface for the np -type geometry. The xy planar average potential is obtained by averaging the raw three-dimensional total potential over the interface plane. The associated macro-averaged smoothed potential is to convolute the xy planar average potential with a Gaussian function using the filtering width $\simeq 0.6\text{\AA}$. As the figure shows, the macro-averaged smoothed potential in SrTiO_3 is flat, indicating that there is no internal electric field through the SrTiO_3 (*i.e.*, it is nonpolar). In the LaAlO_3 layers, the macro-averaged smoothed potential is increasing and lifts up the valence band edge of the capping SrTiO_3 . The energy difference between the O- p states of the SrTiO_3 capping layer and those of the SrTiO_3 substrate increases with increasing LaAlO_3 film thickness. The right column of Fig. 4 shows the

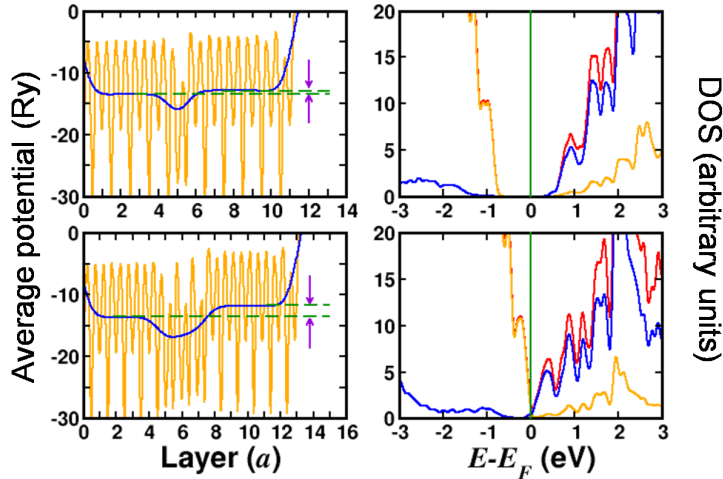


FIG. 4: The average potential (left) and density of states (right) of the np -type interface with different thicknesses. The upper two panels correspond to the np -type interface with 1 unit cell of LaAlO_3 , and the lower two panels correspond to the np -type interface with 3 unit cells of LaAlO_3 . In the right panels, the red, blue, and orange lines are the total density of states (DOS), the atomic projected DOS of Ti- d states, and the atomic projected DOS of O p -states, respectively. The vertical green line in the right panels is the Fermi level.

corresponding density of states (DOS). As the upper panel shows, since the potential increase by 1 unit cell of LaAlO_3 is not large enough to overcome the band gap of SrTiO_3 , the system is still insulating. In the lower panel, the potential increase by 3 unit cells of LaAlO_3 is larger than the band gap of SrTiO_3 , so that the Ti- d states in the SrTiO_3 substrate and O- p states in the capping SrTiO_3 layer overlap. Then the system becomes metallic.

Further evidence of the insulating-to-metallic transition is shown by the local density of states (LDOS) at the Fermi level of the n -type interface in Fig. 5a. From the character of these states, we can see that we have Ti- d states in the SrTiO_3 substrate and O- p states on the surface. Fig. 2 shows the spatial distributions of the conducting electrons and the holes integrated over xy -plane at the n -type and p -type interfaces, respectively. The details of how to extract out these transferred charge densities are provided in Appendix A. From Fig. 2, it is clear that the conducting electrons and holes behave very differently in the SrTiO_3 substrate. The conducting electrons, which occupy Ti- d states, decay away from the n -type

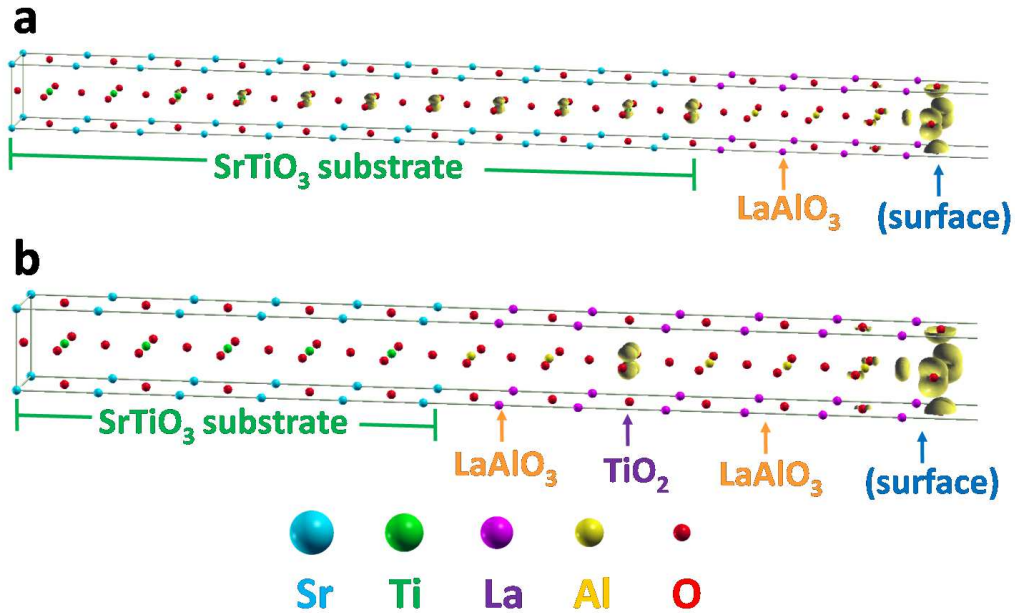


FIG. 5: 3D isovalue surfaces (yellow contour) showing the local density of states at the Fermi level for **a)** the n -type interface and **b)** the new quantum well systems. The conduction electrons (occupying Ti- d orbitals) extend into the SrTiO₃ substrate at the n -type interface, but are localized in the embedded TiO₂ layer at the QW. Holes occupy the O- p states on the surface in both cases.

interface over a length scale of $\simeq 10$ unit cells, indicating that the conducting electron gas is several nm thick. This result is in qualitative agreement with experimental measurements of the superconducting electron gas [9] and other theoretical calculations [16, 30]. Unlike the conducting electrons, the spatial distribution of the holes resembles that of a particle in a box, implying that the holes are very weakly bound to the interface. As elucidated in our previous work [28], the reason for this asymmetry is that the conducting electron gas is trapped at the n -type interface due to a large interfacial hopping matrix element. We will discuss this phenomenon further in Section III C.

2. The quantum well system

Though the conduction electrons are bound to the n -type interface, they still spread over several nanometers. The observed thickness of the electron gas at the n -type interface varies widely in experiments, from nanometers to microns, depending on the growth conditions [44]. Thus it would be desirable to be able to manually control the thickness of the electron

gas. Based on the polar catastrophe mechanism, we propose a new class of quantum well systems that will allow this functionality. The quantum well system, which is illustrated in Fig. 3d, has the following composition: SrTiO₃ substrate/2 u.c. LaAlO₃ / m u.c. SrTiO₃ /LaAlO₃ capping layer, where m can be varied to control the thickness of the conducting electron gas, as we discuss below. Along the (001) direction, this configuration results in three interfaces: one p -type interface between the SrTiO₃ substrate and the 2 u.c. LaAlO₃ buffer layer, and two n -type interfaces on both sides of the inserted thin SrTiO₃ film. Both of the LaAlO₃ thin films are stoichiometric in this system, while the embedded SrTiO₃ thin film is not. As we have two n -type interfaces, the quantum well systems have one extra TiO₂ layer in the inserted SrTiO₃ film. Like the n -type and np -type interfaces, the two SrTiO₃ unit cells of the substrate facing the vacuum are fixed to simulate a bulk-like substrate and all the other atoms are fully relaxed.

The reason that this configuration forms a quantum well can also be explained in terms of an energy diagram. Fig. 3d shows that the polar fields in the two LaAlO₃ thin films point in opposite directions. Therefore, the energy of the Ti- d states in the embedded SrTiO₃ thin film is lowered relative to the conduction band edge of the SrTiO₃ substrate. (We choose two unit cells of LaAlO₃ as the buffer layer in order to bring down the Ti- d states of the embedded SrTiO₃ film into the band gap of the SrTiO₃ substrate). As the capping LaAlO₃ layer thickens, the energy of the O- p states eventually becomes higher than that of the Ti- d states of the embedded SrTiO₃ film, and hence an insulating-to-metallic transition occurs. The difference between the quantum well systems and the n -type interface is that once the insulating-to-metallic transition happens, the conduction electrons get trapped in the Ti- d states of the embedded SrTiO₃ film rather than those of the SrTiO₃ substrate. Therefore, by changing the thickness of the embedded SrTiO₃ film, we can manually control the spatial extent of the electron gas while holding the number of transferred electrons constant. Consequently, we have two parameters to vary: 1) the thickness of embedded SrTiO₃ film to control the spatial extent of electron gas, and 2) the thickness of LaAlO₃ capping layer to control the insulating-to-metallic transition. For simplicity, in the following, we focus on one particular subclass in which the embedded SrTiO₃ is narrowed down to a single TiO₂ layer. The thickness of the LaAlO₃ capping layer will be varied. The quantum wells (QW) in the following refer to this particular subclass.

Like the p -type interface, at this new class of quantum well systems, the energy gap is

not the most direct quantity to monitor for the insulating-to-metallic transition. As the LaAlO_3 capping layer is thin, the energy gap of the QW is the energy difference between the Ti- d states of the embedded TiO_2 layer and the O- p states of the SrTiO_3 substrate, which remains at a constant energy. The more relevant quantity is the energy difference between the Ti- d states of the embedded TiO_2 layer and the O- p states on the surface. We refer to this quantity as the ‘Ti-O energy difference’ in the following. Increasing the thickness of the LaAlO_3 capping layer reduces the Ti-O energy difference until it disappears and electron transfer occurs. The minimum thickness of the LaAlO_3 capping layer that enables this electron transfer is defined as the critical separation of the QW systems.

Table II shows the Ti-O energy difference and the critical separation of the QW systems. The critical separation of the QW coincides with that of the n -type interface, reflecting the fact that the band gap of SrTiO_3 is mainly determined by the Ti- d states and the O- p states. Therefore, the absence of Sr atoms does not change the critical separation. The local density of states at the Fermi level of the QW are shown in Fig. 5b. Unlike the n -type interface, at which the filled Ti d -states extend over ~ 10 unit cells in the SrTiO_3 substrate, the only metallic states in the QW systems are localized in the single embedded TiO_2 layer, as anticipated.

This new class of quantum wells displays a number of appealing properties that are absent at the $\text{LaAlO}_3/\text{SrTiO}_3$ n -type interface. First, the thickness of conduction electrons is controlled by the inserted SrTiO_3 film and can be in principle reduced to a single atomic TiO_2 layer. Second, the electronic properties of the new quantum wells largely depend on the polar structure of LaAlO_3 . Therefore, the SrTiO_3 substrate can be replaced by other materials on which LaAlO_3 can be epitaxially grown, *e.g.* LSAT ($\text{La}_{0.29}\text{Sr}_{0.71}\text{Al}_{0.65}\text{Ta}_{0.35}\text{O}_3$). This provides more choices of substrates on which to grow this new quantum well structure. Finally, the new quantum well serves as a practical way to test the recently proposed hypothesis that some electrons do not contribute to transport due to Anderson localization. Popović *et al.* [37] argued that since all the two dimensional states are Anderson localized by disorder, the electrons that occupy the lowest Ti- d bands do not conduct and therefore the observed sheet carrier density should be much smaller than the $0.5e$ per two-dimensional unit cell predicted by the polar catastrophe mechanism [27]. Nevertheless, it is not trivial to distinguish from which band conduction electrons originate. The thinnest of this new type of quantum wells has only one Ti- d band at the Fermi level, corresponding to the sin-

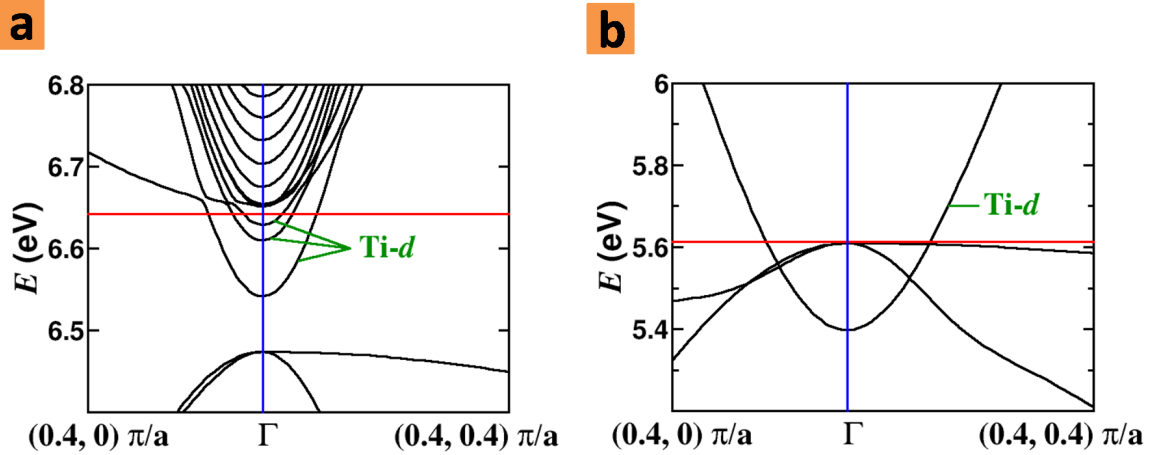


FIG. 6: A comparison of the band structures of **a)** the n -type interface and **b)** the new QW. The n -type interface has 5 unit cells of LaAlO_3 and the QW has a capping layer of 6 unit cells of LaAlO_3 . The red solid line is the Fermi level.

gle embedded TiO_2 layer, which has a strong two-dimensional $\text{Ti-}d_{xy}$ character. Therefore it should show strong localization and not contribute to conductivity. By thickening the embedded SrTiO_3 , one should be changing only the extent of the wave functions and see the localization properties. Fig. 6 shows a comparison of the band structures of the n -type interface and the QW. These two systems both have approximately $0.1e$ per two-dimensional unit cell (from Fig. 9). However, the Fermi level of the n -type interface crosses three $\text{Ti-}d$ bands, while the QW system has only one $\text{Ti-}d$ band at the Fermi level, as expected.

C. Bound versus unbound carriers at the interfaces

In this section, we provide a microscopic picture of the quantum states inhabited by the carriers at the n -type and p -type interfaces, based on a first-principles extraction of tight-binding parameters. As reported in our previous work [28], the main result is that a significant Ti-La interfacial hopping element unique to the n -type interface causes electron to bind there. No such mechanism is operative at the p -type interface, explaining the delocalization of the holes into the SrTiO_3 substrate. As shown below, the Ti-La hopping is significantly enhanced at the n -type interface due to the relatively large size of $\text{La } d$ -orbitals as well as the spatial proximity of the La and Ti atoms in the neighboring atomic planes.

TABLE II: DFT-LDA computed energy gaps and potential changes versus the number of LaAlO₃ layers i for the np -type, n -type and p -type interfaces ($i=0$ refers to a pure SrTiO₃ substrate). Δ is the energy gap of the interface systems (np -type and n -type) with the corresponding number of LaAlO₃ layers. δ is the ‘La-O energy difference’ (p -type interface) or ‘Ti-O energy difference’ (quantum well) with the corresponding number of LaAlO₃ layers. V_i is the macroscopic potential change due to adding the i -th LaAlO₃ layer. Note that ‘La-O energy difference’ is not well defined when $i = 0$ (no LaAlO₃ layer).

np -type			n -type			p -type		QW			
i	Δ (eV)	V_i (eV)	i	Δ (eV)	V_i (eV)	i	δ (eV)	V_i (eV)	i	δ (eV)	V_i (eV)
0	1.85		0	1.85		0	N/A		0	1.85	
1	1.25	0.60	1	1.71	0.14	1	2.59		1	1.83	0.02
2	0.55	0.70	2	1.28	0.43	2	1.89	0.70	2	1.30	0.53
3	metallic		3	0.57	0.71	3	1.18	0.71	3	0.59	0.71
			4	metallic		4	0.49	0.69	4	metallic	
						5	metallic				

Here we provide an expanded and more detailed explanation and analysis of the hopping elements.

To calculate the on-site and hopping matrix elements, we employ Löwdin atomic orbitals [45] where $\langle \mathbf{r} | \alpha \mathbf{R} \rangle = \phi_\alpha(\mathbf{r} - \mathbf{R})$ is a Löwdin orbital of type α localized around lattice position \mathbf{R} . However, as the Kohn-Sham wave functions are Bloch states indexed by wave vectors \mathbf{k} , it is more fruitful to employ Bloch-like superpositions $\varphi_\alpha^{\mathbf{k}}(\mathbf{r})$ defined as

$$\varphi_\alpha^{\mathbf{k}}(\mathbf{r}) = \frac{1}{\sqrt{N_{\mathbf{k}}}} \sum_{\mathbf{R}} e^{i\mathbf{k}\cdot\mathbf{R}} \phi_\alpha(\mathbf{r} - \mathbf{R}). \quad (2)$$

$N_{\mathbf{k}}$ is the total number of k -points in the Brillouin zone sampling. To extract a tight-binding model for the Bloch states at \mathbf{k} , we need to calculate the matrix elements $\langle \varphi_\alpha^{\mathbf{k}} | H | \varphi_\beta^{\mathbf{k}} \rangle$. Making use of the completeness of the Hamiltonian, we obtain:

$$\langle \varphi_\alpha^{\mathbf{k}} | H | \varphi_\beta^{\mathbf{k}} \rangle = \sum_n \langle \varphi_\alpha^{\mathbf{k}} | n\mathbf{k} \rangle E_{n\mathbf{k}} \langle n\mathbf{k} | \varphi_\beta^{\mathbf{k}} \rangle \quad (3)$$

where $\langle \mathbf{r} | n\mathbf{k} \rangle = \psi_{n\mathbf{k}}(\mathbf{r})$ are the actual Bloch eigenstates of the Hamiltonian H . The overlap

$\langle \varphi_\alpha^{\mathbf{k}} | n\mathbf{k} \rangle$ can be recast easily as follows:

$$\langle \varphi_\alpha^{\mathbf{k}} | n\mathbf{k} \rangle = \sqrt{N_{\mathbf{k}}} \int d\mathbf{r} \phi_\alpha^*(\mathbf{r}) \psi_{n\mathbf{k}}(\mathbf{r}) = \langle \alpha\mathbf{0} | n\mathbf{k} \rangle \quad (4)$$

Our final operational formula is

$$\langle \varphi_\alpha^{\mathbf{k}} | H | \varphi_\beta^{\mathbf{k}} \rangle = \sum_n \langle \alpha\mathbf{0} | n\mathbf{k} \rangle E_{n\mathbf{k}} \langle n\mathbf{k} | \beta\mathbf{0} \rangle \quad (5)$$

where the overlaps $\langle \alpha\mathbf{0} | n\mathbf{k} \rangle$ are automatically computed and reported by the PWscf code. Choosing $\alpha = \beta$ gives the on-site energies while $\alpha \neq \beta$ are the hopping elements. The orthonormality relation can also be obtained by replacing H with the identity I operator:

$$\langle \varphi_\alpha^{\mathbf{k}} | \varphi_\beta^{\mathbf{k}} \rangle = \sum_n \langle \alpha\mathbf{0} | n\mathbf{k} \rangle \langle n\mathbf{k} | \beta\mathbf{0} \rangle = \delta_{\alpha\beta} \quad (6)$$

Eq.(6) is a good criterion to check the truncation in the infinite summation over the band index n . In our calculations, we include bands with energies up to 29 eV above the Fermi level, so that $|\langle \varphi_\alpha^{\mathbf{k}} | \varphi_\alpha^{\mathbf{k}} \rangle| > 0.99$ for all Löwdin orbitals considered and $|\langle \varphi_\alpha^{\mathbf{k}} | \varphi_\beta^{\mathbf{k}} \rangle| < 5 \times 10^{-4}$ for all the pairs of two different atomic orbitals.

At the n -type interface, direct projection of the Bloch states $\psi_{n\mathbf{k}}$ onto the atomic orbitals shows that the character of the lowest band accommodating the conduction electrons is mainly Ti- d_{xy} with a small component of La- d_{xy} . The minimum of these occupied bands is at Γ ($\mathbf{k} = \mathbf{0}$). Therefore we build our tight-binding model on the subspace composed of Ti- d_{xy} and La- d_{xy} orbitals and calculate the following on-site and hopping matrix elements:

$$H_{00} = \langle \varphi_{\text{La-}d_{xy}}^\Gamma | H | \varphi_{\text{La-}d_{xy}}^\Gamma \rangle \quad (7)$$

$$H_{jj} = \langle \varphi_{\text{Ti}^j\text{-}d_{xy}}^\Gamma | H | \varphi_{\text{Ti}^j\text{-}d_{xy}}^\Gamma \rangle \quad (8)$$

$$H_{0j} = H_{j0}^* = \langle \varphi_{\text{La-}d_{xy}}^\Gamma | H | \varphi_{\text{Ti}^j\text{-}d_{xy}}^\Gamma \rangle \quad (9)$$

$$H_{ij} = H_{ji}^* = \langle \varphi_{\text{Ti}^i\text{-}d_{xy}}^\Gamma | H | \varphi_{\text{Ti}^j\text{-}d_{xy}}^\Gamma \rangle \quad (10)$$

where ‘La’ in Eq. (7) and Eq. (9) is the La atom in the LaAlO₃ layer at the n -type interface. i (or j) labels the Ti atoms in the SrTiO₃ where $i = 1$ (or $j = 1$) is in the very TiO₂ layer at the n -type interface, and increasing i (or j) refers to the TiO₂ layers that are further away from the interface.

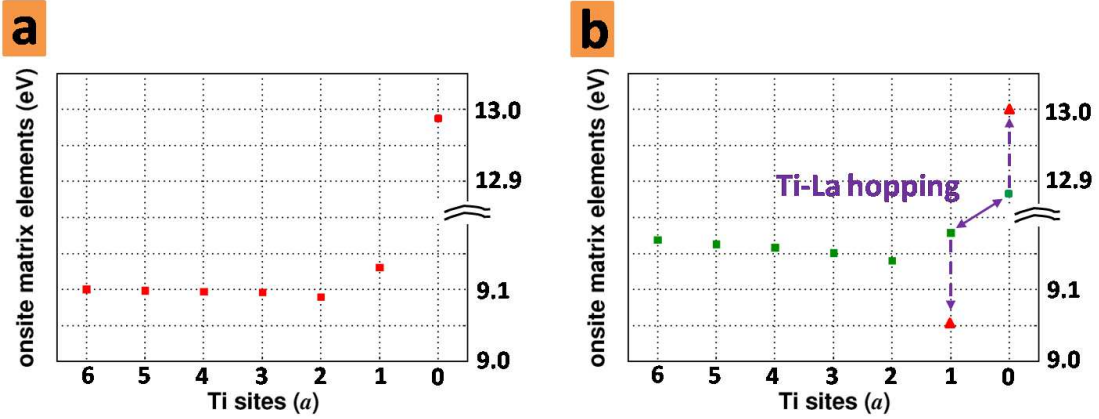


FIG. 7: The on-site matrix elements of the n -type interface. The squares are the on-site matrix elements. Site 0 is the La atom. Sites 1-6 are the Ti atoms. The triangles are the ‘new’ onsite matrix elements after taking into account the hopping effects. The data can be read from Table III. a is the lattice constant of SrTiO_3 . a) The n -type interface with 2 unit cells of LaAlO_3 . b) The n -type interface with 4 unit cells of LaAlO_3 . The purple arrows illustrate the effect of Ti-La hopping as per Eq. (12) and Eq. (13).

The n -type interface with 2 u.c. of LaAlO_3 is insulating (before the polar catastrophe) and that with 4 u.c. of LaAlO_3 is conducting (after the polar catastrophe). Table III shows the on-site and hopping matrix elements of the n -type interface before and after the polar catastrophe, respectively. The on-site matrix elements are also shown in Fig. 7. We can see that the polar catastrophe does not result in significant difference in either the on-site or the hopping matrix elements. Therefore, in the following we mainly focus on the tight-binding Hamiltonian after the polar catastrophe, which is more relevant to describe the conduction electron gas.

Fig. 7 and Table III show that the on-site matrix element of the first Ti atom (closest to the interface) is *not* the lowest one before or after the polar catastrophe; instead, the second Ti atom has the lowest potential. Therefore, one would expect to find the highest electron density on the second Ti atom, in direct contrast to what is actually found in Fig. 2c. However, there is a very large hopping matrix element between the La and Ti atoms at the interface, at least 100 times larger than all the other hopping matrix elements between Ti atoms. This is due to two factors: one is that La-5d orbitals are more extended than Ti-3d orbitals, which leads to a larger overlap, and the other is that the distance between La and Ti

atom at the n -type interface is $\sqrt{3}/2$ times the distance between neighboring Ti atoms [28]. Consequently, to the leading order [56], we neglect the hopping between adjacent Ti atoms and other higher order hopping matrix elements. The Hamiltonian becomes block-diagonal and the only block we need to diagonalize is the leading 2×2 Ti-La submatrix right at the interface:

$$h = \begin{pmatrix} H_{00} & H_{01} \\ H_{10} & H_{11} \end{pmatrix} \quad (11)$$

Diagonalization of Eq. (11) with the tabulated values gives the following eigenvalues and eigenvectors:

$$\varepsilon_1 = 12.99\text{eV}, \quad |\xi_1\rangle = 0.98|\text{La-}d_{xy}\rangle - 0.18|\text{Ti}^1\text{-}d_{xy}\rangle \quad (12)$$

$$\varepsilon_2 = 9.04\text{eV}, \quad |\xi_2\rangle = 0.18|\text{La-}d_{xy}\rangle + 0.98|\text{Ti}^1\text{-}d_{xy}\rangle \quad (13)$$

After diagonalization, we find a pair of bonding and anti-bonding states at the n -type interface. The energy of the binding state ε_2 is even lower than H_{22} , showing that the electrons prefer the Ti site right at the interface. Therefore, after the insulating-to-metallic transition occurs, most electrons reside in this bonding state, which leads to an electron gas bound to the interface. In other words, the large Ti-La hopping matrix element is critical in creating a strongly bound state for the electrons at the interface. Moreover, this hopping is intrinsic to the n -type interface geometry as it does not significantly change its magnitude before and after the polar catastrophe. This also explains the overall similarity of the electron distributions at the symmetric double n -type superlattice (Fig. 2a) and the stoichiometric n -type interface (Fig. 2c). Despite differing in the lack or presence of oppositely charged carriers and polar fields, the two systems share the same Ti-La hopping and thus the same binding force to the interface.

On the other hand, at the p -type interface, holes are found to occupy bands with essentially pure O- p characters and the maximum of those bands is located at M ($\mathbf{k} = (\frac{\pi}{a}, \frac{\pi}{a}, 0)$). The tight-binding model is based on the following matrix elements:

$$H_{ij}^{\mu\nu} = \langle \varphi_{\text{O}^i\text{-}p\mu}^{\text{M}} | H | \varphi_{\text{O}^j\text{-}p\nu}^{\text{M}} \rangle \quad (14)$$

where i, j refer to different O atoms and $\mu, \nu = x, y, z$ refer to different O- p orbitals. We calculate all these matrix elements at the p -type interface before and after the polar catas-

trophe. We find that the hopping elements between nearest neighbor O atoms are all close to 0.6 eV, that there is no order of magnitude difference in the hopping elements, and that there is no discontinuity in going across the p -type interface. This is no surprise because the O atoms form a continuous network across the p -type interface and the hopping matrix elements do not sensitively depend on the nature of the surrounding cations. Therefore, the only difference we expect from the symmetric double p -type results (compare Fig. 2b and Fig. 2d) is that the presence of the polar field at the p -type interface will drive the holes from the LaAlO₃ into the SrTiO₃. However, once in the SrTiO₃, the holes do not feel any strong preference for the interface and therefore diffuse further into the SrTiO₃ substrate. As our calculations have finite film thicknesses, we expect that the profile of holes resembles the lowest state of a free particle in a box and thus have a maximum density in the middle of the film, as borne out by Fig. 2d.

D. Oxygen vacancies repulsion from the interfaces

The theoretical results we have discussed to this point have concerned ideal interfaces with sharp boundaries and 1×1 in-plane periodicity. An important question is whether these assumptions are reasonable for describing the experimentally realized interfaces. This question is obviously very difficult to answer in general as the number of possible ways of perturbing the ideal interfaces is enormous and includes intermixtures, impurities, vacancies, interstitials, off-stoichiometry, etc. Below, we focus on answering one simple but important question for the most prevalent type of imperfections: do oxygen vacancies present in the SrTiO₃ substrate have a strong preference for the SrTiO₃ region close to the interface? Based on both our first principles results and general physical considerations, the answer appears to be no. As we show below, the interface SrTiO₃ region should be relatively free of oxygen vacancies compared to the bulk SrTiO₃ substrate.

Our approach is motivated by experiments that infer a concentration of one oxygen vacancy per four two-dimensional unit cells at the p -type interface [27]. If one assumes each oxygen vacancy donates fully two electrons, this is precisely the amount required to compensate the 0.5 holes per two-dimensional unit cell from the polar catastrophe. The same experiments are also used to infer a non-zero (but smaller) concentration of oxygen vacancies at the n -type interface [27]. To determine the most energetically favorable position

TABLE III: On-site and hopping matrix elements of the n -type interface before and after the polar catastrophe, respectively. l is the thickness of LaAlO_3 . $l = 2$ and 4 unit cells (u.c.) correspond to before and after the polar catastrophe, respectively. We list all the nearest neighbor hopping matrix elements and the largest next nearest neighbor hopping matrix element. The first and third columns are the on-site matrix elements of Ti d -states and hopping matrix elements before the polar catastrophe. The second and fourth columns are the on-site matrix elements of Ti d -states and hopping matrix elements after the polar catastrophe.

i	H_{ii} (eV)		ij	H_{ij} (meV)	
	$l = 2$ u.c.	$l = 4$ u.c.		$l = 2$ u.c.	$l = 4$ u.c.
0	12.99	12.87	0 1	-697	-696
1	9.13	9.18	1 2	-6.39	-1.3
2	9.09	9.14	2 3	-6.80	-0.2
3	9.10	9.15	3 4	-7.03	-0.3
4	9.10	9.19	4 5	-7.07	-0.3
5	9.10	9.16	5 6	-7.07	-0.4
6	9.10	9.17	6 7	-7.05	-0.4
7	9.10	9.18	7 8	-7.03	-0.5
8	9.10	9.19	8 9	-6.98	-0.5
9	9.10	9.19	0 2	-0.87	-7.2

for oxygen vacancies, we compute the formation energy of one monolayer of oxygen vacancies at the same areal density ($1/4$ per two-dimensional unit cell) at various positions inside the SrTiO_3 close to the interface with LaAlO_3 . We perform calculations on both p -type and n -type interfaces using the unit cells shown in Fig. 8.

Our simulation cells include a $2 \times 2 \times 5$ SrTiO_3 film and a $2 \times 2 \times 1$ LaAlO_3 film and $\simeq 25$ Å of vacuum. The substrate termination is SrO in order to minimize any surface effects [28]. The SrTiO_3 unit cell next to the vacuum is fixed to simulate the bulk-like substrate and all the other atoms are relaxed. For a reference, we compute the formation energy of an isolated oxygen vacancy in bulk SrTiO_3 in a $2 \times 2 \times 5$ supercell with one oxygen

vacancy. Starting from the interface, we place the oxygen vacancy in the SrO or TiO₂ layer of the first three SrTiO₃ unit cells and compute the formation energy (see Fig. 8 for the numbering nomenclature of the layers). We show the results in Table IV. As the oxygen vacancies move away from the *p*-type interface, the formation energy decreases, approaching a constant value of 5.4-5.5 eV in the bulk-like regions of the SrTiO₃ films. The computed bulk formation energy is slightly lower (5.18 eV); presumably the small difference is due to the fact that the SrTiO₃ films in the interface geometry are rather thin (only 5 unit cells) and not yet fully in the substrate limit. Nevertheless the energetic *trend* clearly shows the interface region repels the vacancies.

Our results show that there is no energetically favorable binding of oxygen vacancies to either the *p*-type or *n*-type interface. A simple physical picture can explain the repulsion of the oxygen vacancies from both types of interface. An isolated, neutral oxygen vacancy in SrTiO₃ is a donor that binds two electrons (O has formal charge O²⁻). The electrons reside on localized states composed of the *d*-orbitals of the vacancy's surrounding Ti atoms; the energy of these states is close to the SrTiO₃ conduction band edge. Thus, oxygen vacancies can be described as a type of hydrogenic system with bound electrons. As the vacancy approaches the interface, the bound electrons experience what are essentially hard wall boundary conditions since the conduction band edge of LaAlO₃ is ~ 2 eV higher than that of SrTiO₃. As the vacancy approaches the hard wall, its energy increases due to the electron confinement effect [46]. Given the basic physical principles behind this argument, it is clear that it applies to both interfaces. Furthermore, it suggests that even though our first principles results are for relatively high densities of oxygen vacancies in a particular configuration, lower densities and more positionally disordered oxygen vacancies in the SrTiO₃ will still be repelled from the interface region.

The fact that oxygen vacancies are repelled from the interfaces provides a self-consistent picture for our computations of ideal interfaces. Namely, the dominant defects (oxygen vacancies) should not be present in the immediate vicinity of the interfaces. For example, for the *p*-type interface, our theory predicts extended band states for the holes that diffuse substantially into the SrTiO₃ substrate. Since the vacancies are themselves in the bulk of the substrate, they can trap the holes, rendering them immobile. For a relatively thick SrTiO₃ substrate, this situation is likely since only one oxygen vacancy per four two-dimensional unit cells, distributed over the three-dimensional volume of the substrate, is required to

provide the compensating number of electrons.

We would like to comment that experimentally Nakagawa *et al.* [27] found $32 \pm 6\%$ of oxygen vacancies per two-dimensional unit cell at the *p*-type interface. Their conclusion is based on a least-square fit of EELS spectra to the reference spectra of bulk SrTiO₃, bulk LaAlO₃ and oxygen-deficient SrTiO_{3- δ} with $\delta = 1/4$. The discrepancy between our results and those experiments may be due to the following two non-mutually exclusive reasons. One is that in our simulations, we include only one unit cell of LaAlO₃ owing to the computational limitations. More realistic simulations would include thicker LaAlO₃ films to simulate the system after the polar catastrophe when carriers appear in the vicinity of the interfaces. The presence of carriers might in principle affect the formation energy of oxygen vacancies, which needs to be checked in much larger calculations in future work. The other reason is the interpretation of EELS spectra in experiment. The experimental fitting is based on the assumption that any deviation of O-K edge EELS from the bulk SrTiO₃ is caused by the presence of oxygen vacancies. However, even without oxygen vacancies at the *p*-type interface, we observe in our calculations that the atoms close to the interface move away from their bulk positions due to the broken symmetry at the interface. The EELS spectra of the distorted SrTiO₃ could be different from that of the reference bulk structure. Therefore, a more accurate (and more difficult) fit would take into account the deviation of the EELS spectra of distorted SrTiO₃ from the bulk and other possible factors which could also affect the EELS spectra, such as intermixture and nonstoichiometry.

E. Thickness dependence of sheet carrier density

In experiment, the sheet carrier density was observed to display a thickness dependence, but a range of results exist. The sheet carrier density depends on both sample growth conditions and post-annealing [44]. In this section, we present first-principles calculations of the sheet carrier density for different LaAlO₃ film thicknesses. We study the *np*-type, *n*-type and QW systems, and discuss the similarities between these different interface systems.

We define the ‘sheet carrier density’ as the sum of all the conduction electrons per square unit cell in the Ti *d*-states of the SrTiO₃ substrate (for *n*-type and *np*-type interfaces) or in the Ti *d*-states of the single embedded TiO₂ layer (for the QW systems). Fig. 9 shows the sheet carrier density at different thicknesses for all three types of interface. The results

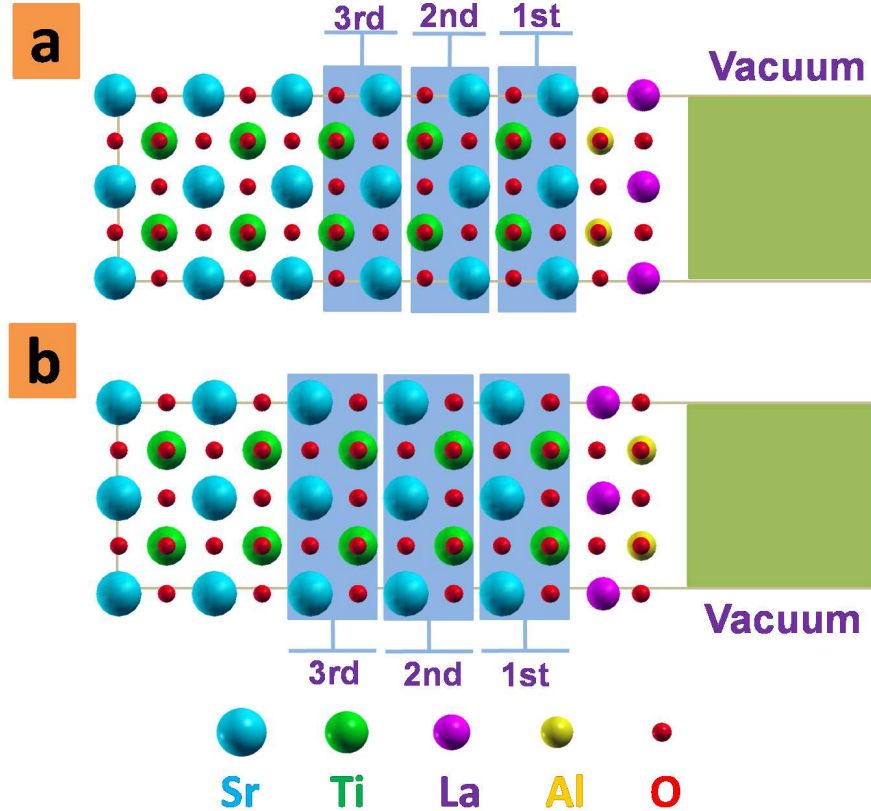


FIG. 8: Schematics of the simulation cell for $\frac{1}{4}$ monolayer oxygen vacancy calculations. One oxygen vacancy is placed in either SrO and TiO₂ of the first, second and third layer, respectively. **a)** The *p*-type interface. **b)** The *n*-type interface.

of *n*-type interface are similar to what Son *et al.* recently obtained [30]. Below the critical separation in each system, there are no mobile carriers since the system is insulating. Above the critical separation, the sheet carrier densities increase in all three cases, following a similar manner. In order to further reveal the similarities among these interface systems, we show in Fig. 10 the relation of the sheet carrier density σ_s versus the internal electric field E through the LaAlO₃. The internal electric field is determined as follows. We calculate the macro-averaged smoothed total potential along the (001) direction. The internal electric field is the slope of the smoothed potential. Though the geometry details differ, the figure shows that the (E, σ_s) relations are almost identical for all three interface types. This suggests that a single continuous model will be able to describe the behavior of all three interfaces. We discuss such a model in Section IV A.

We note that in our calculations of the sheet carrier density, we include all of the electrons

TABLE IV: Formation energies E of $\frac{1}{4}$ monolayer of oxygen vacancy at the p -type and n -type interface. $\frac{1}{4}$ monolayer of oxygen vacancy is in either i th SrO atomic layer or i th TiO₂ atomic layer. For reference, the formation energy in the bulk is 5.18 eV.

p -type		n -type	
position of oxygen vacancy	E (eV)	position of oxygen vacancy	E (eV)
1st SrO layer	6.25	1st TiO ₂ layer	5.65
1st TiO ₂ layer	5.85	1st SrO layer	5.65
2nd SrO layer	5.69	2nd TiO ₂ layer	5.56
2nd TiO ₂ layer	5.56	2nd SrO layer	5.46
3rd SrO layer	5.60	3rd TiO ₂ layer	5.57
3rd TiO ₂ layer	5.50	3rd SrO layer	5.41

in the conduction bands, regardless of whether they in fact contribute to the observed conductivity or not. We find that after the critical separation, the sheet carrier density increases continuously with the thickness of the LaAlO₃ film, asymptoting to $0.5 e/a^2$. This behavior qualitatively agrees with some experiments [5, 23], but conflicts with others [4], in which the sheet carrier density remains almost constant (15 times smaller than $0.5 e/a^2$) after the critical separation. It is possible that the low sheet carrier density in Ref. [4] may be explained in terms of Anderson localization induced by disorder [30, 37].

F. External Field Effect

We have shown that there is an insulating-to-metallic transition as a function of LaAlO₃ thickness both in the SrTiO₃/LaAlO₃ interface and the quantum well (QW) systems. In this section, we examine the effects of inducing this transition at subcritical thicknesses via an applied electric field. We focus on the n -type interface and the QW system with 3 u.c. of LaAlO₃ (for both systems, the critical separation is 4 u.c. in the DFT simulations). To study the field effect, we apply a homogeneous electric field perpendicular to the interface. In order to avoid artificial effects from periodic boundary conditions (see Appendix B), we apply two electric fields of equal magnitude and opposite direction to each half of a

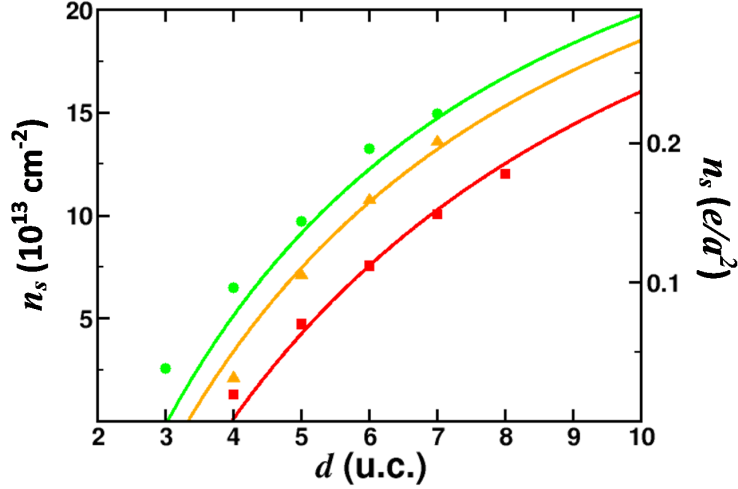


FIG. 9: Comparison of the sheet carrier density computed with the continuous model (see Section IV A) and DFT simulations. The red, orange and green lines are the model calculations of the QW, the n -type and the np -type interfaces, respectively. The squares, triangles and circles are the DFT results of the QW, the n -type and the np -type interfaces, respectively.

symmetric simulation cell (see Fig. 11). Since the system is mirror symmetric, for simplicity we only focus on half of the simulation cell. At the n -type interface, the external electric field is parallel to the intrinsic electric field through the LaAlO_3 film, and in the QW systems, the direction is parallel to the field through the LaAlO_3 capping layer. Based on the polar catastrophe picture, such external electric fields will add to intrinsic electric fields and further reduce the energy gap, so that the insulating-to-metallic transition will occur at a subcritical separation.

We performed the simulations with different magnitudes of external electric field on both the n -type interface and QW systems. We need to elucidate a subtle point here: in the QW, the external electric field reduces the energy difference between the Ti d -states of the embedded TiO_2 layer and O p -states on the surface. This is the ‘Ti-O energy difference’ introduced in Section III B 2. Once this energy difference disappears, the insulating-to-metallic transition occurs. This energy difference is well defined because we can identify two Bloch states, one which characterizes the Ti d -states of the embedded TiO_2 layer and the other which characterizes the O p -states on the surface, and simply take their energy difference. At the n -type interface, the external electric field also reduces the energy difference between the Ti

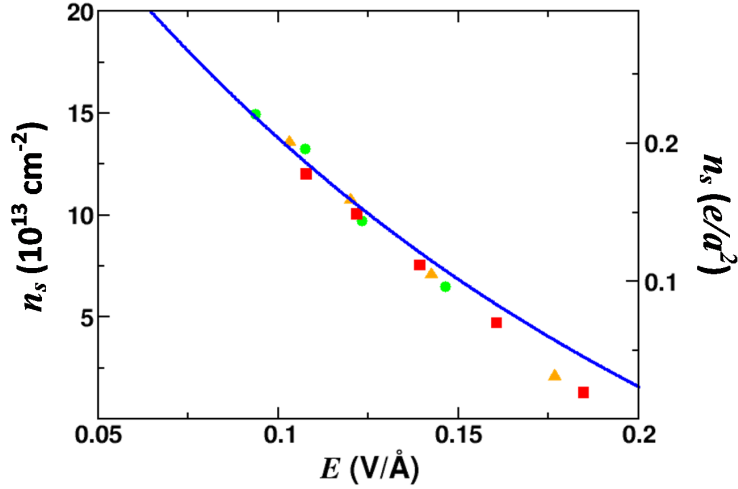


FIG. 10: The sheet carrier density versus the internal electric field through the LaAlO₃ thin film. The red squares, orange triangles, and green circles are for the quantum well, the n -type, and the np -type interfaces, respectively. The blue line is the result of the continuous model described in Section IV A .

d -states of the first Ti atom at the interface and the O p -states on the surface. However, this energy difference is not easily identified because the external electric field also exists throughout the SrTiO₃ substrate, so the Bloch states that accept the transferred electrons are now composed of a mixture of all the Ti d -states in the SrTiO₃ thin film. For the purposes of this section, we simply extract the energy gap of this n -type interface system (between the O p -states on the surface and the lowest occupied Ti d -states) versus the external field. In Section IV B, we will discuss more fully the relation of this energy gap and what would happen in an actual experiment.

In Fig. 12 we show the computed energy gap of the n -type interface and the Ti-O energy difference of the QW as a function of external electric field. As the figure shows, both monotonically decrease with increasing external electric field. Thus, the DFT simulations demonstrate how an external electric field can induce an insulating-to-metal transition.

IV. CONTINUOUS MODEL

In order to shed more light on the nature of the LaAlO₃/SrTiO₃ interface, we develop a simple model which approximates the LaAlO₃ film as a homogeneous continuous medium.

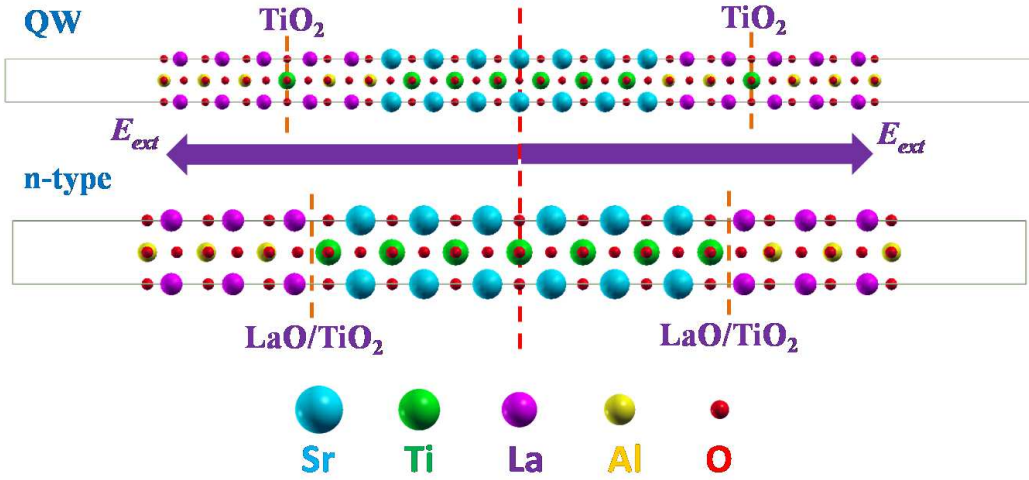


FIG. 11: The supercells used for the field effect calculations. For the QW and the n -type interface, both simulation cells are mirror-symmetric. The external electric field is also mirror-symmetric. The dashed line in the middle is the symmetry axis. The embedded TiO_2 layer in the QW and the n -type interface LaO/TiO_2 are also highlighted by the dashed line.

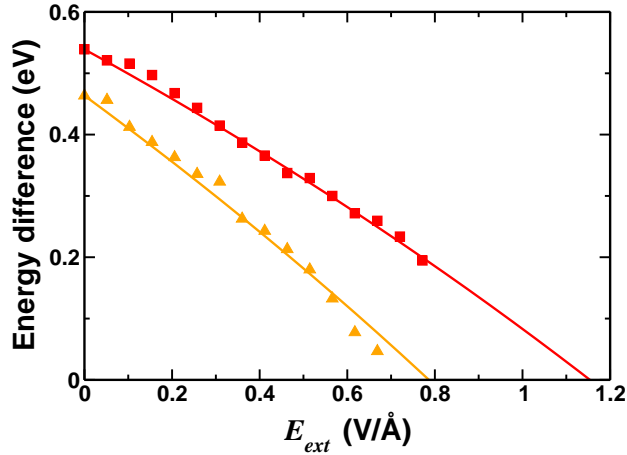


FIG. 12: Energy differences versus the external electric field. The red squares and orange triangles correspond to the DFT-computed Ti-O energy difference for the QW systems and the energy gap of the n -type interface, respectively. The solid lines are the results of the continuous model described in Section IV B.

This model shows that the polar and dielectric properties of LaAlO_3 largely determine the thickness dependence of the sheet carrier density and the external field effect behavior.

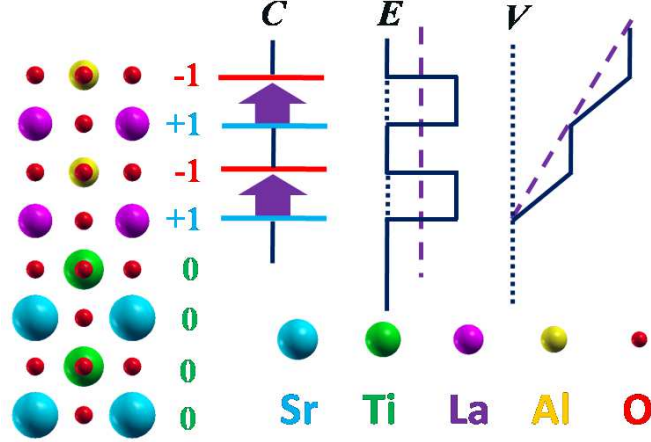


FIG. 13: Schematic illustration of the continuous model. In the ionic limit, the LaAlO_3 thin film can be considered as a serial connection of capacitors. The electric field through LaAlO_3 is like an impulse and the resulting potential takes a stair shape. The dashed purple lines are the average electric field and the average potential.

A. Thickness dependence of sheet carrier density

In this section, we use model calculations, aided by DFT results, to quantitatively describe the insulating-to-metallic transition that occurs at the n -type and np -type interfaces and the quantum well (QW) systems. As detailed below, we find that the electric field dependence of ϵ_L is critical in obtaining quantitative accuracy.

Before the insulating-to-metallic transition occurs, the alternating positively charged $(\text{LaO})^+$ and negatively charged $(\text{AlO}_2)^-$ layers in the LaAlO_3 film can be idealized as a series of capacitors (see Fig. 13). As the figure illustrates, the thickness of each capacitor is only half of the unit cell of LaAlO_3 (there is zero voltage drop across the other half). Therefore the inner electric field through the LaAlO_3 behaves like an impulse and the resulting potential takes the shape of a stair function. If we approximate the LaAlO_3 thin film as a continuous homogeneous media and average this electric field, we can determine the average internal electric field:

$$\overline{E} = \frac{1}{2} \frac{4\pi\sigma_0}{\epsilon_L} = \frac{4\pi\overline{\sigma}}{\epsilon_L}, \quad (15)$$

where $\sigma_0 = e/a^2$ is an electron per two-dimensional unit cell, ϵ_L is the dielectric constant of

LaAlO₃, and

$$\bar{\sigma} = \frac{\sigma_0}{2} = \frac{e}{2a^2}. \quad (16)$$

Once the insulating-to-metallic transition occurs, some electrons transfer across the interface to counteract the internal electric field through the LaAlO₃ thin film. The new average internal electric field through the LaAlO₃ film is then given by:

$$\bar{E} = \frac{4\pi(\bar{\sigma} - \sigma_s)}{\epsilon_L}, \quad (17)$$

where σ_s is the transferred electron density, or sheet carrier density. It is easy to recast Eq. (17) into:

$$\sigma_s(\bar{E}) = \bar{\sigma} - \frac{\bar{E}\epsilon_L}{4\pi}, \quad (18)$$

where $\bar{\sigma} = 0.5e/a^2$. We also take into account that the dielectric constant ϵ_L depends on the internal electric field \bar{E} . The field dependence can be phenomenologically described by the Landau theory, and takes the following approximate form [47, 48] (also see Appendix C):

$$\epsilon_L(\bar{E}) \simeq \epsilon_0 \left(1 + \left(\frac{\bar{E}}{\mathcal{E}_0} \right)^2 \right)^{-1/3}, \quad (19)$$

where ϵ_0 is the dielectric constant of LaAlO₃ at vanishing electric field and \mathcal{E}_0 is a characteristic electric field. Eq. (18) and Eq. (19) establish a relation between the internal electric field \bar{E} through the LaAlO₃ and the sheet carrier density σ_s , both of which can be calculated independently from DFT simulations. We also performed a separate slab calculation (see Appendix C 1 for details) and determined the parameters ϵ_0 and \mathcal{E}_0 in Eq. (19) as:

$$\epsilon_0 = 40.95, \quad \mathcal{E}_0 = 0.15\text{V}/\text{\AA} \quad (20)$$

Fig. 10 compares (E, σ_s) computed via DFT and the model. We can see from Fig. 10 that (E, σ_s) almost lies on the same curve in all three cases, which does not depend on the details of the structure. The continuous model shows a good agreement with the DFT results, and as the internal electric field decreases (i.e. the thickness of the LaAlO₃ increases), the continuous model becomes almost exact. This is expected because in the limit of an infinitely thick LaAlO₃ film, the interface and surface regions become negligible. Our results show

that even with only 7 u.c. of LaAlO_3 (*i.e.* the internal electric field $< 0.12 \text{ V/\AA}$), the continuous model already works very well.

However, it is not easy to directly measure the internal electric field through the LaAlO_3 experimentally because the LaAlO_3 film is only a few unit cells thick. It is more useful to relate the sheet carrier density to the nominal thickness of the LaAlO_3 film (*i.e.* the number of LaAlO_3 unit cells grown on top of the SrTiO_3 substrate). Therefore, we need to find how the internal electric field through the LaAlO_3 depends on the LaAlO_3 thickness.

When the polar catastrophe takes place at the n -type interface, electrons leave the surface O - p states and are transferred into the Ti - d states. The charge transfer is halted once a common Fermi level is reached. Approximately, this means that the Ti - d conduction band edge of the SrTiO_3 substrate is at the same energy as the O - p surface valence band edge. Looking back at Fig. 3, we can see that there is a remanent field through the LaAlO_3 film and thus a potential difference. The existence of the electric field is also visible in Fig. 10 from our calculations. The potential difference across the LaAlO_3 thin film, denoted by K , can be related to the remanent internal electric field by:

$$e\overline{E}d = K \quad (21)$$

where d is the thickness of LaAlO_3 . In principle K could depend on the thickness of LaAlO_3 . But the detailed calculations show (see Fig. 14) that K quickly saturates to a constant as the thickness d gets larger. This could be understood because K is essentially determined by the energies of the relevant electronic states and the band offsets, which are interface properties and have little dependence on the thickness of LaAlO_3 . We therefore approximate K as a constant. We illustrate later that this approximation does not significantly change the physics in the continuous model.

Inserting Eq. (21) into Eq. (18) and Eq. (19), we eliminate \overline{E} and obtain:

$$\sigma_s = \overline{\sigma} - \frac{K}{4\pi ed} \epsilon_0 \left(1 + \left(\frac{K}{e\mathcal{E}_0 d} \right)^2 \right)^{-1/3} \quad (22)$$

Eq. (22) highlights some qualitative features of the sheet carrier density. The critical separation is the smallest d which makes $\sigma_s > 0$. Below the critical separation, the sheet carrier density is zero. Above the critical separation, the sheet carrier density gradually increases and then saturates to $\overline{\sigma} = 0.5e/a^2$ in the limit of large d .

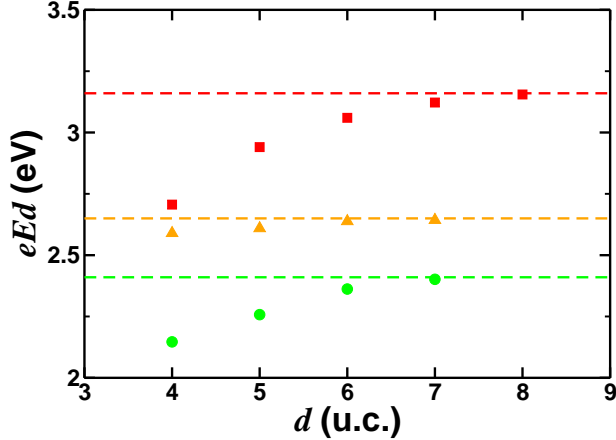


FIG. 14: The potential difference across the LaAlO_3 thin film, defined by $e\bar{E}d$, of the quantum well (QW), the n -type and the np -type interfaces. Squares, triangles, and circles correspond to the QW, the n -type, and the np -type interfaces, respectively. \bar{E} is the average internal electric field along the (001) direction through the LaAlO_3 thin film and d is the nominal number of LaAlO_3 unit cells (note that the SrTiO_3 -strained LaAlO_3 lattice constant $a_{\text{LAO}} = 0.953a_{\text{STO}}$). The dashed lines highlight the data point of the largest thickness in each interface configuration.

The parameter K in Eq. (22) is determined as follows. We simulate n -type, np -type interfaces and QW with different thicknesses and calculate the macro-averaged smoothed electric field through the LaAlO_3 at each thickness. In Fig. 14, we show the potential difference across the LaAlO_3 thin film, defined by $e\bar{E}d$. We can see that in all three cases, $e\bar{E}d$ quickly saturates as d gets larger. Since we do not have a microscopic model to describe how the potential difference $e\bar{E}d$ changes with the thickness d , we use the last data (corresponding to the largest d) to determine the values of K , which are highlighted by the dashed line in Fig. 14. In each case, we find that

$$K_{\text{QW}} = 3.16 \text{ eV}, \quad K_n = 2.64 \text{ eV}, \quad K_{np} = 2.40 \text{ eV}. \quad (23)$$

The K in all three cases turn out to be different from each other and larger than the DFT-computed band gap of SrTiO_3 (1.85 eV). This is partly because the band offsets of these three cases are not the same. However, the small valence band offsets alone [13, 15] can not explain the big difference between the K value and SrTiO_3 band gap. A more important factor is that we treat \bar{E} as a uniform electric field throughout the LaAlO_3 thin film. However, close

to the interface and surface, the internal electric field should be different from that in the middle of the LaAlO_3 film but difficult to average in those regions. Therefore we use an approximate relation ($K = e\overline{E}d$) to determine the potential difference, but as shown later, this approximation is good enough to reproduce the DFT-calculated thickness dependence of sheet carrier density.

Equipped with K , ϵ_0 and \mathcal{E}_0 , we can calculate the sheet carrier density at different thicknesses using Eq. (22). We compare the sheet carrier densities calculated from the continuous model with those from the DFT simulations. The results are shown in Fig. 9. The agreement is good in all three cases even though Eq. (21) is not exact.

We would like to comment that recently Son *et al.* [30] also calculated the thickness dependence of sheet carrier density and they made a similar model by assuming that the dielectric constant of LaAlO_3 has no field dependence and is simply constant. Rather than Eq.(22), they had a simpler formula

$$\sigma_s = \overline{\sigma} \left(1 - \frac{d_c}{d} \right) \quad (24)$$

where $\overline{\sigma}$ and d_c are two constants determined by fitting. They found $\overline{\sigma} = 0.455e/a^2$, close to the ideal value $0.5e/a^2$. Our analysis is different in that we fix $\overline{\sigma} = 0.5e/a^2$, which is necessitated by the polar catastrophe mechanism, but take into account that the dielectric constant of LaAlO_3 has a strong field dependence, as confirmed by the DFT calculations.

B. External electric field

In order to get a more quantitative description of the external field effect, we apply the continuous model established in the previous section. In principle, at the subcritical separation (3 u.c.), the continuous model should break down because the LaAlO_3 film is so thin that the interface and surface regions cannot be neglected and the LaAlO_3 is no longer uniform. However, we simplify the situation by assuming that LaAlO_3 is still a homogeneous media with the dielectric constant given by Eq. (19) with the parameters Eq. (20), but has an effective thickness d_{eff} . In order to simplify our notations, we use E instead of \overline{E} to denote the averaged macroscopic fields.

Based on the above argument, for the quantum well systems we have:

$$\Delta = \Delta_0 - (E^L - E_0^L)d_{eff}^L, \quad (25)$$

where ‘ L ’ stands for LaAlO_3 . Δ is the Ti-O energy difference at a given E_{ext} and E^L is the internal electric field. Δ_0 and E_0^L indicate the values of Δ and E^L , respectively, at vanishing external electric field:

$$E^L = \frac{4\pi\bar{\sigma} + E_{ext}}{\epsilon_L(E^L)} \quad (26)$$

and

$$E_0^L = \frac{4\pi\bar{\sigma}}{\epsilon_L(E_0^L)} \quad (27)$$

Equations (25, 26, and 27) establish the relation between Δ and E_{ext} . The effective thickness cannot be given *a priori* from the model. Instead, we fit the data and find $d_{eff}^L = 5.9\text{\AA} = 1.6$ u.c. A comparison of (E_{ext}, Δ) for the quantum well systems using DFT calculations and the model calculations is shown in Fig. 12.

For the n -type interface, we also need to account for the potential drop in the SrTiO_3 due to the external electric field. Therefore we have:

$$\Delta = \Delta_0 - (E^L - E_0^L)d_{eff}^L - E^S d_{eff}^S \quad (28)$$

where ‘ S ’ stands for SrTiO_3 . Δ is the energy gap of the system and Δ_0 is the value of Δ at vanishing external electric field. Note that in the absence of an external electric field, the SrTiO_3 film is unpolarized in the continuous model. E^S and E_{ext} are related by:

$$E^S = \frac{E_{ext}}{\epsilon_S(E^S)} \quad (29)$$

We use the Berry phase method [49] to calculate $\epsilon_S(E)$ and fit the data using Eq. (19) (see Appendix C 2 for details). The results of the fit are:

$$\epsilon_0^S = 309.6, \mathcal{E}_0^S = 49.2\text{V}/\mu\text{m} = 4.92 \times 10^{-3}\text{V}/\text{\AA} \quad (30)$$

We find that the values of d_{eff}^L in different systems are different. Hence, in principle we have two fitting parameters in Eq. (28): d_{eff}^L and d_{eff}^S . However, it turns out that Eq. (28) very insensitively depends on d_{eff}^S . This is expected because the dielectric constant of SrTiO_3 is

at least 10 times larger than that of LaAlO₃ and the nominal thicknesses of LaAlO₃ and SrTiO₃ are both 3 u.c. in the DFT calculations (see Fig. 11), and thus the potential drop across the SrTiO₃ is much smaller than that across the LaAlO₃ film. Therefore we just use the real thickness of SrTiO₃ $d_{eff}^S = 11.1 \text{ \AA}$ (from the relaxed structure) and fit the data with d_{eff}^L . We find: $d_{eff}^L = 7.5 \text{ \AA} \simeq 2 \text{ u.c.}$ Fig. 12 compares the values of (E_{ext}, Δ) of the n -type interface computed by DFT and the model, respectively.

Fig. 12 shows that the critical electric fields E_{ext}^c extracted from the DFT calculations for the n -type interface and the QW are 0.79 and 1.15 V/Å, respectively. In the continuous model, the critical voltage across the whole sample is given by:

$$V_c = \frac{E_{ext}^c + 4\pi\bar{\sigma}}{\epsilon_{LAO}}d_{LAO} + \frac{E_{ext}^c}{\epsilon_{STO}}d_{STO} \quad (31)$$

where d_{LAO} and d_{STO} are the thickness of LaAlO₃ and SrTiO₃, respectively. $\bar{\sigma} = 0.5e/a^2$ and E_{ext}^c is the critical external electric field. In order to estimate the critical voltage for the experimental setup, we need to use the thickness of the SrTiO₃ substrate in experiment.

Here we need to clarify some subtleties: in the presence of applied external field, DFT simulations do not realistically represent the spatial distribution of conduction electrons. Fig. 15 illustrates the reason for the discrepancy. In the DFT simulations, the conduction electrons fill the lowest energy states. Since the “external” field bends the SrTiO₃ conduction bands, these states are located at the bottom surface of the SrTiO₃ substrate, as shown schematically in Fig. 15a. Although in principle the experimental situation is the same, realistically, electrons can only tunnel a few unit cells from the surface; thus they get trapped at the n -type interface, as illustrated in Fig. 15b. The trapping mechanism is the Ti-La interfacial hopping, which lowers the energy of the Ti atom closest to the interface and creates the energy barrier through which the electrons must tunnel. Hence, the real critical field has to be larger than the computed one, so that the energy of surface states equals that of the interface states (Fig. 15b). The critical external field E_{ext}^c we obtain from DFT simulations is therefore only a lower bound.

Now we make a simple estimation of the lower bound: at low temperatures ($< 5 \text{ K}$), the dielectric constant of SrTiO₃ can be as large as 2.5×10^4 [50] and the thickness of the SrTiO₃ substrate is typically $\simeq 1 \text{ mm}$. Considering that $\epsilon_{LAO} \simeq 30$ and $d_{LAO} \simeq 10 \text{ \AA}$, the second term in Eq.(31) is dominant. Therefore, for the n -type interface, we have:

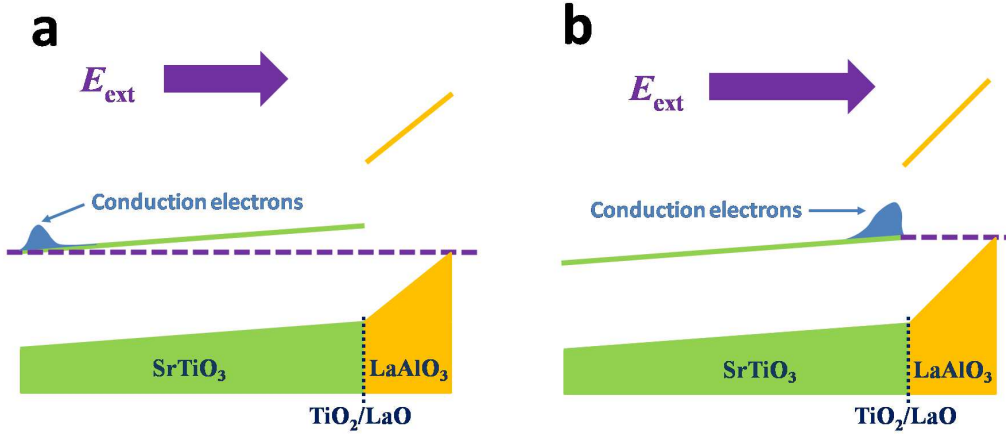


FIG. 15: **a)** The spatial distribution of conduction electrons in the DFT simulations. The conduction electrons occupy the lowest energy states available, which are located at the bottom surface. **b)** The spatial distribution of conduction electrons in the actual experiment. The conduction electrons get trapped at the n -type interface by the tunneling barrier due to the self-consistent potential well formed at the interface that largely stems from the Ti-La hopping. The length of arrows illustrates the magnitude of external field.

$$V_c^{n\text{-type}} \simeq \frac{E_{ext}^c}{\epsilon_{STO}} d_{STO} \simeq 320 \text{ V} \quad (32)$$

and for the QW,

$$V_c^{QW} \simeq \frac{E_{ext}^c}{\epsilon_{STO}} d_{STO} \simeq 480 \text{ V} \quad (33)$$

As these estimates are based on data from DFT simulations in which the band gap of SrTiO₃ is underestimated, they provide only lower bounds on the critical voltage. Experimentally, the critical voltage of the n -type interface with a 1 mm thick SrTiO₃ substrate has been measured to be $\simeq 70$ V at low temperature [4], which is much smaller than our estimates. The discrepancy may imply that the simple model of an ideally sharp interface is not sufficient to model the external field doping, due to additional details that play an important role at the n -type interface. Various types of atomic reconstructions, such as cation intermixtures at the interface [27] or oxygen vacancies on the surface [10] may possibly trigger an insulating-to-metallic transition, leading to a smaller critical voltage.

V. CONCLUSION

We present a detailed study of ideal $\text{LaAlO}_3/\text{SrTiO}_3$ interfaces and a new class of quantum wells. In both systems, we confirm an intrinsic insulating-to-metallic transition. The observed transition can be triggered either by thickening the LaAlO_3 layers or by imposing an external electric field, both of which can be explained by the polar catastrophe mechanism. We show that for both the n -type interface and QW, the realistic critical separation (taking into account the underestimation of DFT band gap) is around 6 unit cells. We also show that, given a typical SrTiO_3 substrate thickness of 1mm, the lower bound for the critical voltage necessary to induce an insulating-to-metallic transition is estimated to be ~ 300 V for the ideal n -type interface and ~ 500 V for the QW. In addition to theoretically demonstrating the observed physical properties, we provide a microscopic explanation of the observed binding of conduction electrons at the n -type interface, a phenomenon which can not be described by the polar catastrophe mechanism alone. We demonstrate that the large La-Ti hopping matrix element at the n -type interface, which is absent in both bulk constituents and is unique to the n -type interface, lowers the energy of the Ti atom at the interface relative to all other Ti sites, thus binding the electrons. Furthermore, we develop a continuous model that captures the essence of polar structure and dielectric properties and predicts the thickness dependence of sheet carrier densities.

We conclude by discussing some of the outstanding issues related to this system. Our understanding of the atomically sharp interfaces and QW suggests that the electronic properties of $\text{LaAlO}_3/\text{SrTiO}_3$ interfaces observed in experiments are unlikely to be solely a result of electronic reconstructions based on the polar catastrophe mechanism. For example, the theoretical critical separation, predicted by the polar catastrophe picture, is 6 u.c. [18, 28–30], which is larger than the experimental value (4 u.c.) [4]. In addition, while the calculated thickness dependence of the sheet carrier density agrees qualitatively with some experiments [5, 23] in that the sheet carrier density increases with LaAlO_3 thickness, it disagrees with other experiments [4] which show an almost constant sheet carrier density above the critical separation. The sheet carrier density we calculate here includes all the conduction electrons. Whether some of them may be prone to the Anderson localization [37] is an issue beyond the scope of the DFT calculations. However, the possibility of multiple type of carriers [51] is an interesting question that warrants further study in both theory and experiment.

Another remaining puzzle is that the polar catastrophe predicts the coexistence of electrons at the interface and holes on the surface, while experiments find that the surface region is insulating and only electron-like carriers are detected in the transport measurement [4]. Recently, x-ray photoemission measurement found that the polar field through LaAlO_3 is much smaller than the theoretical predictions [42]. It is possible that various atomic reconstructions, such as cation intermixing, nonstoichiometry and defects could also significantly affect the electronic structures of these interface systems and be partially responsible for the discrepancies mentioned above. While a detailed discussion of atomic reconstructions is beyond our present work, it serves as an interesting direction for future research.

Appendix A: Conduction electron and hole densities

In this appendix, we explain how we calculate the *conduction* electron and hole densities for the symmetric superlattices and stoichiometric interface systems. The basic tool we use is the local density of states (LDOS) for the system

$$D(\mathbf{r}, E) = \sum_{n\mathbf{k}} |\psi_{n\mathbf{k}}(\mathbf{r})|^2 \delta(E - \epsilon_{n\mathbf{k}}) \quad (\text{A1})$$

which we integrate over the appropriate energy range.

1. Double *n*-type and *p*-type superlattices

The symmetric nonstoichiometric double *n*-type (*p*-type) superlattice is shown in Fig. 1a (Fig. 1b). The corresponding electron (hole) density is presented in Fig. 2a (Fig. 2b). For the symmetric superlattices, there is no polar field and analysis of the density of states shows that there is an easily identifiable energy gap at all locations in the film; the Fermi level is either above the conduction band edge for the *n*-type superlattice or below the conduction band for the *p*-type superlattice. For the transferred electron density (Fig. 2a), we integrate the LDOS from the middle of the band gap to the Fermi level,

$$\eta(\mathbf{r}) = \int_{\mathcal{E}}^{E_F} D(\mathbf{r}, E) dE \quad (\text{A2})$$

where \mathcal{E} is the energy in the middle of the band gap. We are in fact counting all the electrons in the conduction bands. For the transferred hole density (Fig. 2b), similarly we integrate

the LDOS from the Fermi level to the middle of the band gap,

$$\xi(\mathbf{r}) = \int_{E_F}^{\mathcal{E}} D(\mathbf{r}, E) dE \quad (\text{A3})$$

i.e. counting all the holes in the valence bands. The integrated LDOS $\eta(\mathbf{r})$ and $\xi(\mathbf{r})$ are then averaged over the xy plane and finally plotted along the z direction.

2. Stoichiometric n -type and p -type interface systems

The stoichiometric n -type (p -type) interface system is shown in Fig. 3b (Fig. 3c). The corresponding *conduction* electron (hole) density is shown in Fig. 2c (Fig. 2d). For the stoichiometric n -type and p -type interfaces, the polar field ensures that the bands edges in the LaAlO_3 are not flat and that the Fermi level will intersect the band edges of the SrTiO_3 as well as the surface of the LaAlO_3 film (see Fig. 3). However, the local density of states in the SrTiO_3 film still clearly shows a band gap. Therefore, we can also compute the transferred charges at the interface using the above formula. The only complication is that in addition to showing the transferred charges in the interface region, $\eta(\mathbf{r})$ and $\xi(\mathbf{r})$ will necessarily have contributions localized at the surface region of LaAlO_3 which are not of direct interest when studying the interface alone; the choice of axis range in Fig. 2c and 2d effectively excludes this contribution. As a consistency check, we can also compute the transferred charge by computing the atomic projections of all Bloch states in the system and identifying all those states with the proper atomic character: Ti- d or La- d character and partial occupancy for the n -type interface, and O- p character and partial occupancy for the p -type interface. One can then manually sum up these particular contributions to get the electron and hole distributions, and the results agree with the previous method in the relevant regions.

Appendix B: Periodic boundary condition effects

When we perform a slab calculation, the materials in the simulation are generally polarized either due to intrinsic polar fields (*e.g.* LaAlO_3) or external electric fields. In DFT calculations, the periodic boundary conditions (PBC) imposed on the simulation cell influence the screening properties of the materials. We will show in the following two sections

that the presence of PBCs does not significantly affect the polarization due to intrinsic polar fields in the system, but it does induce large artificial effects when one studies the response of the system to an external field, requiring a careful set up of the simulation and interpretation of the results.

1. Polarization due to intrinsic fields

In this section, we illustrate that in the SrTiO₃/LaAlO₃ interface system, PBCs induce an artificial field through SrTiO₃, but we show that this effect is negligible.

As shown in Fig. 16a, the two boundary conditions of displacement \mathbf{D} at each interface give:

$$D_{\text{LAO}} - D_{\text{STO}} = 4\pi\sigma \quad (\text{B1})$$

$$D_{\text{STO}} - D_{\text{V}} = 0 \quad (\text{B2})$$

PBCs require that the total potential drop over the whole simulation cell is equal to zero:

$$E_{\text{STO}}s + E_{\text{LAO}}l + E_{\text{V}}v = 0 \quad (\text{B3})$$

where s , l and v are the thicknesses of SrTiO₃, LaAlO₃ and vacuum, respectively. Considering that $E_i = D_i/\epsilon_i$ (i is SrTiO₃, LaAlO₃ or vacuum), we can solve D_{STO} and D_{LAO} explicitly,

$$D_{\text{STO}} = -4\pi\sigma \frac{l/\epsilon_{\text{LAO}}}{s/\epsilon_{\text{STO}} + l/\epsilon_{\text{LAO}} + v/\epsilon_{\text{V}}} \quad (\text{B4})$$

$$D_{\text{LAO}} = 4\pi\sigma \frac{s/\epsilon_{\text{STO}} + v}{s/\epsilon_{\text{STO}} + l/\epsilon_{\text{LAO}} + v/\epsilon_{\text{V}}} \quad (\text{B5})$$

The dielectric constants of SrTiO₃, LaAlO₃ and vacuum are roughly:

$$\epsilon_{\text{STO}} \simeq 300 \gg \epsilon_{\text{LAO}} \simeq 25 \gg \epsilon_{\text{V}} = 1 \quad (\text{B6})$$

and the thicknesses of SrTiO₃, LaAlO₃ and vacuum in the simulation cell are on the same order of magnitude (within a factor of two), therefore we have the following simplifications:

$$E_{\text{LAO}} \simeq \frac{4\pi\sigma}{\epsilon_{\text{LAO}}} \quad (\text{B7})$$

$$E_{\text{STO}} \simeq -\frac{4\pi\sigma}{\epsilon_{\text{LAO}}\epsilon_{\text{STO}}}\frac{l}{v} = -\frac{l}{v\epsilon_{\text{STO}}}E_{\text{LAO}} \rightarrow |E_{\text{STO}}| \ll |E_{\text{LAO}}| \quad (\text{B8})$$

$$E_{\text{V}} \simeq -\frac{4\pi\sigma}{\epsilon_{\text{LAO}}}\frac{l}{v} = -\frac{l}{v}E_{\text{LAO}} \rightarrow E_{\text{V}}v \simeq -E_{\text{LAO}}l \quad (\text{B9})$$

Eq. (B8) and Eq. (B9) show that though SrTiO₃ is artificially polarized due to the PBCs, the electric field through SrTiO₃ is much smaller than the intrinsic field through LaAlO₃ and the voltage built across the LaAlO₃ film mostly drops in the vacuum. Based on the above approximate dielectric constants, the field in SrTiO₃ is only $\sim 0.3\%$ of that in LaAlO₃. In addition, we can further reduce the field in SrTiO₃ by increasing the thickness of the vacuum v ; the above relations give a quantitative measure of the (small) error for any finite value of v .

2. Polarization due to an applied external electric field

We illustrate in this section that when we use a slab calculation and a sawtooth potential to simulate an external electric field through nonpolar materials (*e.g.* SrTiO₃), PBCs will artificially undermine the screening and give rise to a significantly smaller dielectric constant.

Fig. 16b shows a schematic of how an external electric field E_{ext} along the z direction is screened in a nonpolar material. There are two induced electric fields. The one in the material is the standard depolarization field E_{dep} and the other field, which we call the outside field E_{out} , is in the vacuum with the opposite direction. E_{ext} , E_{dep} and E_{out} are the *magnitudes* of each field; their directions are explicitly shown in Fig. 16b. We denote the size of the unit cell along the z direction by L and the thickness of the slab by d . The sawtooth potential automatically satisfies the periodic boundary condition (the reversed part is not shown in Fig. 16b). Therefore, the induced electric fields required to satisfy the periodic boundary condition are given by:

$$E_{\text{dep}}d = E_{\text{out}}(L - d) \quad (\text{B10})$$

On the other hand, Gauss's law gives:

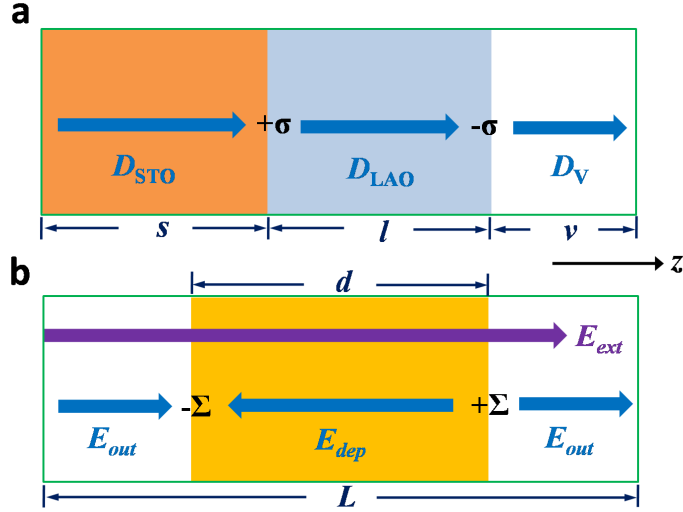


FIG. 16: Schematics of how the periodic boundary condition affects the screening of the electric fields. **a)** Polarization due to intrinsic fields. The shaded parts are SrTiO₃ and LaAlO₃, respectively. The interface is *n*-type. The unshaded part denotes vacuum. **b)** Polarization due to an applied electric field. The shaded part is a general nonpolar material and the empty part is vacuum.

$$4\pi\Sigma = E_{dep} + E_{out} \quad (\text{B11})$$

where the surface charge density Σ is related to the polarization in the material by

$$\Sigma = \mathbf{n} \cdot \mathbf{P} = P \quad (\text{B12})$$

and the polarization P is related to the total electric field E_{tot} by

$$P = \chi E_{tot} \quad (\text{B13})$$

where χ is the permittivity. From Fig. 16b, it is easy to see that

$$E_{tot} = E_{ext} - E_{dep} \quad (\text{B14})$$

Combining Eq. (B10-B14) gives

$$E_{tot} = \frac{E_{ext}}{1 + 4\pi\chi\left(1 - \frac{d}{L}\right)} \quad (\text{B15})$$

Now we can identify the dielectric constant ϵ

$$\epsilon = \frac{E_{ext}}{E_{tot}} = 1 + 4\pi\chi \left(1 - \frac{d}{L}\right) \quad (\text{B16})$$

Eq. (B16) is different from the familiar formula $\epsilon = 1 + 4\pi\chi$ in that we have an extra factor $(1 - d/L)$. In typical slab calculations $(1 - d/L) \sim 30\%$ and for high- k materials (*e.g.* SrTiO₃) $\chi \gg 1$ so that ϵ is dominated by the second term in Eq. (B16) and thus the reduction factor is a significant error.

3. A remedy

The origin of the deviation of the dielectric constant from the correct value of $1 + 4\pi\chi$ is that the electric field induced by the bound charge $\pm\Sigma$ does not completely serve as the depolarization field, but is instead split into two parts, E_{dep} and E_{out} . The presence of E_{out} is purely due to the imposed periodic boundary condition, and is unphysical. However, in practical slab calculations it is too computationally expensive to make d/L small.

In order to get rid of E_{out} , we need a simulation cell in which the depolarization field automatically satisfies periodic boundary conditions. Therefore, we use a mirror-symmetric simulation cell in which the external electric field is also mirror-symmetrically distributed. By symmetry, E_{dep} automatically satisfies periodic boundary conditions and E_{out} is guaranteed to be zero in the vacuum. Thus, the external electric field is correctly screened, but with a relatively modest increase in computational expense due to doubling the simulation cell along one direction.

Appendix C: Field dependence of dielectric constant

The Landau theory phenomenologically describes the field dependence of the dielectric constant [47, 48]. It is assumed that the free energy of the system $F(P, T)$ can be expanded in even powers of the polarization P :

$$F(P, T) = F_0 + AP^2 + BP^4 + CP^6 + \dots \quad (\text{C1})$$

where the coefficients $A, B, C\dots$ may depend on the temperature T . Keeping only terms in F to the fourth order, we obtain:

$$E = \frac{\partial F}{\partial P} = 2AP + 4BP^3 \quad (\text{C2})$$

and the permittivity follows:

$$\frac{1}{\chi} = \frac{\partial E}{\partial P} = 2A + 12BP^2 \quad (\text{C3})$$

Eq. (C2) and Eq. (C3) uniquely determine $\chi = \chi(P)$ and $P = P(E)$. The analytical solution to Eq. (C2) $P = P(E)$ is complicated, but we can find a useful interpolation scheme [47, 48] by noting that as P is small, $\chi \rightarrow (2A)^{-1}$ and as P is large, $\chi \propto P^{-2}$ and $E \propto P^3$, that is $\chi \propto E^{-2/3}$, so

$$\chi \simeq \chi_0 \left(1 + \left(\frac{E}{\mathcal{E}_0} \right)^2 \right)^{-1/3} \quad (\text{C4})$$

For high- k materials, we can also approximate $\epsilon \simeq 4\pi\chi \gg 1$, giving the final expression:

$$\epsilon \simeq \epsilon_0 \left(1 + \left(\frac{E}{\mathcal{E}_0} \right)^2 \right)^{-1/3} \quad (\text{C5})$$

where ϵ_0 and \mathcal{E}_0 are fitting parameters.

We note that the truncation of Eq. (C1) is based on the assumption that P is small (*i.e.* E is small). However, the Landau theory itself does not give a characteristic polarization or electric field. Instead, we consider \mathcal{E}_0 as a characteristic electric field whose value is determined by the fitting. Thus, data points much larger than \mathcal{E}_0 should not be used in the fitting because Eq. (C1) would break down. This is a self-consistent check.

1. LaAlO₃

Before we calculate the dielectric constant ϵ_L of LaAlO₃, we need to elucidate a subtle point. The ϵ_L we calculate here is only well defined in the thin slab of LaAlO₃, not in the bulk. This is because we are in the region of very strong electric field ($\sim 0.7 \text{ V}/a_{\text{LAO}}$). With a few unit cells, the potential difference built across the slab will be larger than the band gap of LaAlO₃, and Zener tunneling will occur. Bulk LaAlO₃ can not accommodate such a large electric field and the Berry phase method [49] for calculating the dielectric constant breaks down in this regime. Instead, we resort to a mirror-symmetric slab calculation (see

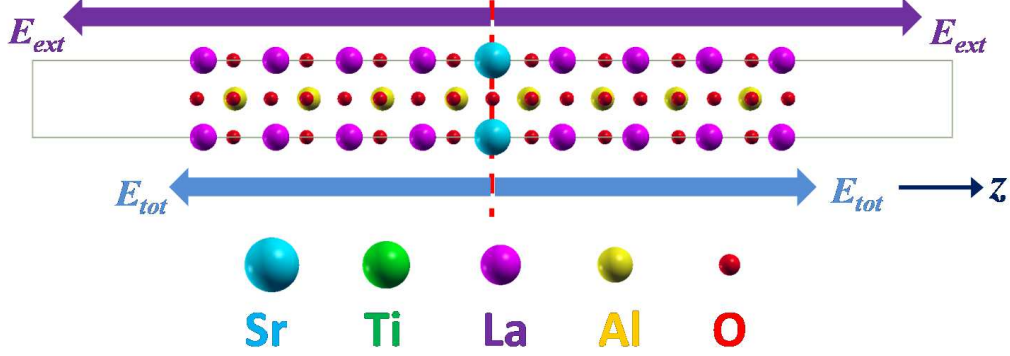


FIG. 17: Schematics of the simulation cell of LaAlO_3 slab calculations. Both the simulation cell and the external electric field are mirror-symmetric. All fields through LaAlO_3 are along the z direction (perpendicular to the interface).

Fig. 17 and Appendix B). We turn on a mirror-symmetric external electric field E_{ext} and calculate the macro-averaged electric field E_{tot} through the material. The dielectric constant is then defined as:

$$\epsilon_L(E_{tot}) = \frac{E_{ext}}{E_{tot}} \quad (\text{C6})$$

The raw data and the fitting curve using Eq. (C5) are shown in Fig. 18. The fitting results are:

$$\epsilon_0 = 40.95, \quad \mathcal{E}_0 = 0.15\text{V}/\text{\AA} \quad (\text{C7})$$

2. SrTiO_3

Since SrTiO_3 is a nonpolar material with a large dielectric constant, the typical internal electric field through SrTiO_3 is much smaller than that through LaAlO_3 . The dielectric constant we are interested in can be defined in the bulk (based on the argument of metastable states) and calculated using the Berry phase method. In order to accurately determine the atom positions, we use $6 \times 6 \times 20$ k -point sampling and lower the force convergence threshold to $8 \text{ meV}/\text{\AA}$. We directly calculate the total polarization P_{tot} (both ionic and electronic) in the unit cell at a given total electric field E_{tot} and the dielectric constant follows straightforwardly:

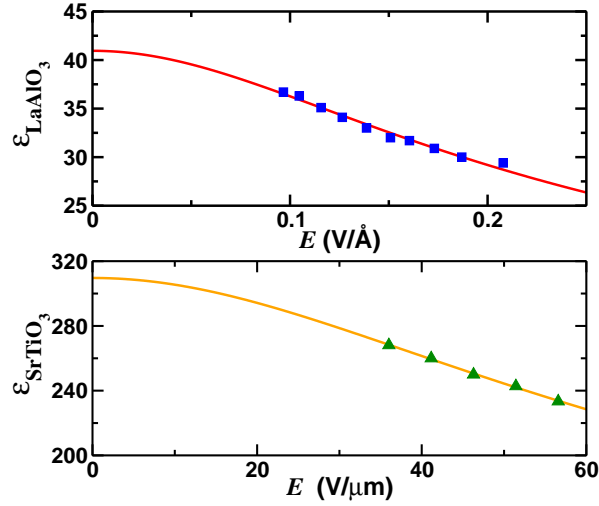


FIG. 18: Electric field dependence of dielectric constants of LaAlO₃ and SrTiO₃. The solid squares are the results of the slab calculations and the solid triangles are the results of Berry phase calculations. The solid lines are the fitting results using Eq. (C5).

$$\epsilon_S(E_{tot}) = 4\pi \frac{P_{tot}}{\Omega E_{tot}} + 1 \quad (C8)$$

where Ω is the volume of unit cell. The raw data and fitting curve are shown in Fig. 18, with the fitting results:

$$\epsilon_0^S = 309.6, \mathcal{E}_0^S = 49.2\text{V}/\mu\text{m} = 4.92 \times 10^{-3}\text{V}/\text{\AA} \quad (C9)$$

-
- [1] E. Dagotto, *Science* **318**, 1076 (2007).
 - [2] M. Kawasaki, K. Takahashi, T. Maeda, R. Tsuchiya, M. Shinohara, O. Ishiyama, T. Yonezawa, M. Yoshimoto, and H. Koinuma, *Science* **266**, 1540 (1994).
 - [3] A. Ohtomo and H. Y. Hwang, *Nature* **427**, 423 (2004).
 - [4] S. Thiel, G. Hammerl, A. Schmehl, C. W. Schneider, and J. Mannhart, *Science* **313**, 1942 (2006).
 - [5] M. Huijben, G. Rijnders, D. H. A. Blank, S. Bals, S. V. Aert, J. Verbeeck, G. V. Tendeloo, A. Brinkman, and H. Hilgenkamp, *Nature Mater.* **5**, 556 (2006).
 - [6] C. Bell, S. Harashima, Y. Hikita, and H. Y. Hwang, *Appl. Phys. Lett.* **94**, 222111 (2009).

- [7] A. D. Caviglia, S. Gariglio, N. Reyren, D. Jaccard, T. Schneider, M. Gabay, S. Thiel, G. Hammerl, J. Mannhart, and J. M. Triscone, *Nature* **456**, 624 (2008).
- [8] A. Brinkman, M. Huijben, M. V. Zalk, J. Huijben, U. Zeitler, J. C. Maan, W. G. V. der Wiel, G. Rijnders, D. H. A. Blank, and H. Hilgenkamp, *Nature Mater.* **6**, 493 (2007).
- [9] N. Reyren, S. Thiel, A. D. Caviglia, L. F. Kourkoutis, G. Hammerl, C. Richter, C. W. Schneider, T. Kopp, A. S. Rüetschi, D. Jaccard, et al., *Science* **317**, 1196 (2007).
- [10] C. Cen, S. Thiel, G. Hammerl, C. W. Schneider, K. E. Andersen, C. S. Hellberg, J. Mannhart, and J. Levy, *Nature Mater.* **7**, 298 (2008).
- [11] C. Cen, S. Thiel, J. Mannhart, and J. Levy, *Science* **323**, 1026 (2009).
- [12] R. Pentcheva and W. E. Pickett, *Phys. Rev. B* **74**, 035112 (2006).
- [13] R. Pentcheva and W. E. Pickett, *Phys. Rev. B* **78**, 205106 (2008).
- [14] M. S. Park, S. H. Rhim, and A. J. Freeman, *Phys. Rev. B* **74**, 205416 (2006).
- [15] J. M. Albina, M. Mrovec, B. Meyer, and C. Elsässer, *Phys. Rev. B* **76**, 165103 (2007).
- [16] K. Janicka, J. P. Velev, and E. Y. Tsymbal, *Phys. Rev. Lett.* **102**, 106803 (2009).
- [17] Z. Zhong and P. J. Kelly, *Europhys. Lett.* **84**, 27001 (2008).
- [18] J. Lee and A. A. Demkov, *Phys. Rev. B* **78**, 193104 (2008).
- [19] P. R. Willmott, S. A. Pauli, R. Herger, C. M. Schlepütz, D. Martoccia, B. D. Patterson, B. Delley, R. Clarke, D. Kumah, C. Cionca, et al., *Phys. Rev. Lett.* **99**, 155502 (2007).
- [20] A. Kalabukhov, R. Gunnarsson, J. Börjesson, E. Olsson, T. Claeson, and D. Winkler, *Phys. Rev. B* **75**, 121404(R) (2007).
- [21] G. Herranz, M. BasletiĆ, M. Bibes, C. CarrÉtero, E. Tafra, E. Jacquet, K. Bouzouane, C. Deranlot, A. HamziĆ, J. M. Broto, et al., *Phys. Rev. Lett.* **98**, 216803 (2007).
- [22] W. Siemons, G. Koster, H. Yamamoto, W. A. Harrison, G. Lucovsky, T. H. Geballe, D. H. A. Blank, and M. R. Beasley, *Phys. Rev. Lett.* **98**, 196802 (2007).
- [23] M. Sing, G. Berner, A. M. K. Goß, A. Ruff, A. Wetscherek, S. Thiel, J. Mannhart, S. A. Pauli, C. W. Schneider, P. R. Willmott, et al., *Phys. Rev. Lett.* **102**, 176805 (2009).
- [24] M. Salluzzo, J. C. Cezar, N. B. Brookes, V. Bisogni, G. M. D. Luca, C. Richter, S. Thiel, J. Mannhart, M. Huijben, A. Brinkman, et al., *Phys. Rev. Lett.* **102**, 166804 (2009).
- [25] S. Thiel, C. W. Schneider, L. F. Kourkoutis, D. A. Muller, N. Reyren, A. D. Caviglia, S. Gariglio, J.-M. Triscone, and J. Mannhart, *Phys. Rev. Lett.* **102**, 046809 (2009).
- [26] J. N. Eckstein, *Nature Mater.* **6**, 473 (2007).

- [27] N. Nakagawa, H. Y. Hwang, and D. A. Muller, *Nature Mater.* **5**, 204 (2006).
- [28] H. Chen, A. M. Kolpak, and S. Ismail-Beigi, *Phys. Rev. B* **79**, 161402 (2009).
- [29] R. Pentcheva and W. E. Pickett, *Phys. Rev. Lett* **102**, 107602 (2009).
- [30] W. joon Son, E. Cho, B. Lee, J. Lee, and S. Han, *Phys. Rev. B* **79**, 245411 (2009).
- [31] M. Basletic, J.-L. Mauric, C. Carrétéro, G. Herranz, O. Copie, M. Bibes, E. Jacquet, K. Bouzouhane, S. Fusil, and A. Barthélémy, *Nature Mater.* **7**, 621 (2008).
- [32] M. C. Payne, M. P. Teter, D. C. Allan, T. A. Arias, and J. D. Joannopoulos, *Rev. Mod. Phys.* **64**, 1045 (1992).
- [33] W. Kohn and L. J. Sham, *Phys. Rev.* **140**, A1133 (1965).
- [34] D. Vanderbilt, *Phys. Rev. B* **41**, 7892 (1990).
- [35] S. Gemming and G. Seifert, *Acta Mater.* **54**, 4299 (2006).
- [36] K. Janicka, J. P. Velev, and E. Y. Tsymbal, *J. Appl. Phys.* **103**, 07B508 (2008).
- [37] Z. S. Popović, S. Satpathy, and R. M. Martin, *Phys. Rev. Lett.* **101**, 256801 (2008).
- [38] J. Lee and A. A. Demkov, *Mater. Res. Soc. Symp. Proc.* **0966-T07-33** (2007).
- [39] M. Peressi, N. Binggeli, and A. Baldereschi, *J. Phys. D* **31**, 1273 (1998).
- [40] A. Baldereschi, S. Baroni, and R. Resta, *Phys. Rev. Lett.* **61**, 734 (1988).
- [41] L. Colombo, R. Resta, and S. Baroni, *Phys. Rev. B* **44**, 5572 (1991).
- [42] Y. Segal, J. H. Ngai, J. W. Reiner, F. J. Walker, and C. H. Ahn, *Phys. Rev. B* **80**, 241107 (2009).
- [43] R. Pentcheva, M. Huijben, K. Otte, W. E. Pickett, J. E. Kleibeuker, J. Huijben, H. Boschker, D. Kockmann, W. Siemons, G. Koster, et al. (2009), URL [arXiv.org:0912.4671](http://arxiv.org/0912.4671).
- [44] H. Chen, A. Kolpak, and S. Ismail-Beigi, *Adv. Mater.* (to appear) (2010).
- [45] P.-O. Löwdin, *J. Chem. Phys.* **18**, 365 (1950).
- [46] S. Satpathy, *Phys. Rev. B* **28**, 4585 (1983).
- [47] A. F. Devonshire, *Philos. Mag.* **40**, 1040 (1949).
- [48] A. Antons, J. B. Neaton, K. M. Rabe, and D. Vanderbilt, *Phys. Rev. B* **71**, 024102 (2005).
- [49] I. Souza, J. Íñiguez, and D. Vanderbilt, *Phys. Rev. Lett.* **89**, 117602 (2002).
- [50] M. A. Saifi and L. E. Cross, *Phys. Rev. B* **2**, 677 (1970).
- [51] S. S. A. Seo, Z. Marton, W. S. Choi, G. W. J. Hassink, D. H. A. Blank, H. Y. Hwang, T. W. Noh, T. Egami, and H. N. Lee, *Appl. Phys. Lett.* **95**, 082107 (2009).
- [52] See <http://www.quantum-espresso.org>

- [53] Some atoms are fixed in order to simulate the bulk-like substrate. This is specified in each section.
- [54] See the EPACS Document No. E-PRBMDO-79-R12912 for a detailed discussion of surface effects of TiO_2 termination.
- [55] Detailed calculations show that the surface states have character of La $5d$, $6s$ and $6p$.
- [56] We in fact perform the exact diagonalization and find that neglecting the hopping between adjacent Ti atoms and other higher order hopping matrix elements is an excellent approximation. More importantly, this leading order approximation described in the text shows that the Ti-La hopping is crucial in trapping the electrons at the n -type interface.